

# Tensor-based computation of metastable and coherent sets

Recent years have seen rapid advances in the data-driven analysis of dynamical systems based on Koopman operator theory – with extended dynamic mode decomposition (EDMD) being a cornerstone of the field. On the other hand, low-rank tensor product approximations – in particular the tensor train (TT) format – have become a valuable tool for the solution of large-scale problems in a number of fields. In this work, we combine EDMD and the TT format, enabling the application of EDMD to high-dimensional problems in conjunction with a large set of features. We derive efficient algorithms to solve the EDMD eigenvalue problem based on tensor representations of the data, and to project the data into a low-dimensional representation defined by the eigenvectors. We extend this method to perform canonical correlation analysis (CCA) of non-reversible or time-dependent systems. We prove that there is a physical interpretation of the procedure and demonstrate its capabilities by applying the method to several benchmark data sets.

Keywords: Extended dynamic mode decomposition, canonical correlation analysis, data-driven regression problems, tensor networks, tensor-train format, higher-order decomposition methods, molecular dynamics

MSC: 15A69, 37L65, 37M10, 62H20, 92C40

## Feliks Nüske

Center for Theoretical  
Biological Physics,  
Department of Chemistry,  
Rice University,  
Houston, TX, 77005,  
United States

Institute of Mathematics,  
Universität Paderborn,  
Paderborn 33100,  
Germany

## Patrick Geiß

Department of  
Mathematics and  
Computer Science,  
Freie Universität Berlin,  
Berlin 14195, Germany

## Stefan Klus

Department of  
Mathematics and  
Computer Science,  
Freie Universität Berlin,  
Berlin 14195, Germany

## Cecilia Clementi

Center for Theoretical  
Biological Physics,  
Department of Chemistry,  
Rice University,  
Houston, TX, 77005,  
United States

## 1 Introduction

The data-driven analysis of high-dimensional dynamical systems has been a highly successful research field for several years, with applications in fluid dynamics, control theory, molecular dynamics, and many others. Most of the work along these lines has focused on the infinite-dimensional description of a system using *transfer operators* or *Koopman operators*, see [1, 2, 3, 4], which we will summarily call *evolution operators* in this paper. A host of different methods for the numerical approximation of evolution operators from simulation or measurement data have been developed, see [5] for a review and comparison. A particularly important contribution is the *extended dynamic mode decomposition* (EDMD) [6, 7], which will be the focus of this study. For reversible dynamical systems, EDMD is equivalent to the *variational approach to conformational dynamics* (VAC) [8, 9]. For non-reversible or time-dependent systems, it turned out that considering a *forward-backward operator* is more appropriate. The spectral analysis of the forward-backward operator leads to the detection of *coherent sets* [10, 11], which can be achieved by an algorithm called *canonical correlation analysis* (CCA), see [12, 13].

Much of the appeal of these techniques is due to their formulation as data-driven regression problems, which opens the door to the application of modern machine learning techniques. Examples include kernel-based formulations [14, 15] and combinations with deep learning [16]. A different avenue towards the solution of high-dimensional problems are tensor products, where functions on high-dimensional spaces are approximated in linear spaces of products of simple (often univariate) functions. The expansion coefficients of such a function form a multi-dimensional array, called a *tensor*. As the size of a tensor grows exponentially with the dimension, *low-rank formats* requiring only a manageable number of parameters need to be used. Important examples include the *canonical format* [17], the *Tucker format* [18], and the *hierarchical Tucker format* [19],

with the *tensor train (TT) format* [20, 21] as an important special case of the latter. The common idea behind these formats is to decompose a high-dimensional tensor into a network of lower-dimensional tensors. Several applications of tensor decompositions have shown that it is possible to tackle large-scale problems which cannot be solved using conventional numerical methods, see, e.g., [22, 23, 24, 25, 26], and especially [27, 28, 29] for quantum chemistry applications.

Low-rank approximations have also been used in the context of EDMD. The *Nyström method* was discussed in [30] for the matrix case. For a tensor product basis, it was shown in [31] that the Galerkin matrices for the Perron–Frobenius or Koopman operator can directly be written in the canonical format. The resulting generalized eigenvalue problems can be converted to TT format and then solved with the aid of power iteration methods. This, however, requires repeated rank reductions and appropriate estimates of the eigenvalues so that power iteration quickly converges. A different approach to tensor-based EDMD, based on the alternating least squares method, was suggested in [32].

In this study, we apply tensor decompositions on the level of the *data tensor*, which contains the evaluations of a product basis at all data points. We build on the *AMUSE* algorithm [33] for the solution of the EDMD eigenvalue problem. AMUSE only requires a *singular value decomposition* (SVD) of the data matrix followed by the solution of a standard matrix eigenvalue problem. Recent work [34] has shown that such an SVD can also be computed for data matrices in TT format. The detailed contributions of our study are then as follows:

- First, we present an alternative tensor train decomposition of the data tensor corresponding to a product basis. It is based on a greedy method outlined in [35], which provides a *higher-order CUR decomposition*. A detailed description of the latter method’s algorithmic realization, including several enhancements, is provided.
- Second, we derive the tensor train version of AMUSE, called *AMUSE<sub>t</sub>*, and show that the resulting standard matrix eigenvalue problem can be set up efficiently due to orthonormality properties of the SVD.
- Third, we show that *AMUSE<sub>t</sub>* can be modified to perform CCA, which corresponds to computing eigenfunctions of the forward-backward operator.
- Fourth, we show that *AMUSE<sub>t</sub>* in fact reduces the problem to performing EDMD or CCA within a subspace of the full tensor space, thus retaining a physical interpretation of the procedure. We also prove that this subspace converges in the infinite data limit.
- Finally, we demonstrate the capabilities of the proposed methods by analyzing benchmark data sets of molecular dynamics simulation and fluid dynamics.

The remainder of this work is structured as follows: In Section 2, we introduce the required notation and concepts, in particular Galerkin approximations of evolution operators, tensor decompositions, and higher-order tensor decompositions. The main algorithmic and theoretical contributions are presented in Section 3. Numerical results for benchmark problems are then shown in Section 4, and concluding remarks and open problems follow in Section 5.

## 2 Basic Concepts

In this section, we recapitulate basic concepts from dynamical systems theory and from numerical linear algebra required for the rest of the paper. First, we introduce the Galerkin approximation of evolution operators for dynamical systems in Section 2.1. Afterwards, we change topics and discuss low-rank approximations of tensors in the tensor train format in Section 2.2. The two strands will be connected in Section 3. Throughout the paper, vector spaces will be denoted by blackboard bold symbols (e.g.,  $\mathbb{R}, \mathbb{V}$ ), unless standard symbols like  $L^2$  are used.

## 2.1 Evolution operators

This study is concerned with the analysis of dynamical systems. Let  $\mathcal{X}_t \in \mathbb{R}^d$  be a deterministic or stochastic dynamical system. For a positive lag time  $\tau$  and densities  $\rho_0, \rho_1$ , the Perron-Frobenius operator  $\mathcal{T}_\tau: L^2_{\rho_0} \rightarrow L^2_{\rho_1}$  is defined by

$$\mathcal{T}_\tau f(y) = \frac{1}{\rho_1(y)} \int f(x) \rho_0(x) p^\tau(x, y) dx, \quad (1)$$

where  $p^\tau$  is the stochastic transition kernel associated with the process  $\mathcal{X}_t$ . If the process admits an invariant distribution  $\mu$ , it is convenient to choose  $\rho_0 = \rho_1 = \mu$ . In particular, if the dynamics  $\mathcal{X}_t$  are reversible with respect to  $\mu$ , the operator  $\mathcal{T}_\tau$  is self-adjoint on  $L^2_\mu$ . However, an invariant measure may not always exist, especially if the dynamics are not time-homogeneous. In general, the adjoint of  $\mathcal{T}_\tau$  is the Koopman operator

$$\mathcal{K}_\tau f(x) = \int p^\tau(x, y) f(y) dy, \quad (2)$$

and it is identical to  $\mathcal{T}_\tau$  on  $L^2_\mu$  in the reversible case.

For finite-dimensional spaces  $\mathbb{V} \subset L^2_{\rho_0}$  and  $\mathbb{W} \subset L^2_{\rho_1}$  with bases  $\psi_1, \dots, \psi_n$  and  $\phi_1, \dots, \phi_n$ , respectively, the Galerkin approximations to the operators  $\mathcal{K}_\tau$  and  $\mathcal{T}_\tau$  are given by matrices

$$K^\tau = (C^{00})^+ \cdot C^{01}, \quad T^\tau = (C^{11})^+ \cdot C^{10}, \quad (3)$$

with  $C_{ij}^{00} = \langle \psi_i, \psi_j \rangle_{\rho_0}$ ,  $C_{ij}^{01} = \langle \psi_i, \mathcal{K}_\tau \phi_j \rangle_{\rho_0}$ ,  $C_{ij}^{10} = \langle \phi_i, \mathcal{T}_\tau \psi_j \rangle_{\rho_1}$ , and  $C_{ij}^{11} = \langle \phi_i, \phi_j \rangle_{\rho_1}$ , see [5, 7].

### 2.1.1 Extended Dynamic Mode Decomposition

Usually, the integrals required for the matrices in (3) cannot be computed analytically, and are estimated from data instead. Assume we have data  $x_k$ , for  $k = 1, \dots, m$ , sampled from  $\rho_0$ , and their time-lagged counterparts  $y_k$ , obtained by integrating the dynamics over time  $\tau$  starting from  $x_k$ . Assembling all pairs into data matrices  $X, Y \in \mathbb{R}^{d \times m}$ , where  $X = [x_1, \dots, x_m]$  and  $Y = [y_1, \dots, y_m]$ , we define the *transformed data matrices* in  $\mathbb{R}^{n \times m}$  by

$$\Psi(X) = [\psi(x_1) \ \dots \ \psi(x_m)] \quad \text{and} \quad \Psi(Y) = [\phi(y_1) \ \dots \ \phi(y_m)]. \quad (4)$$

Empirical estimates of  $C^{00}$ ,  $C^{01}$ ,  $C^{10}$  and  $C^{11}$  are then given by  $\widehat{C}^{00} = \Psi(X) \cdot \Psi(X)^\top$ ,  $\widehat{C}^{01} = \Psi(X) \cdot \Psi(Y)^\top$ ,  $\widehat{C}^{10} = \Psi(Y) \cdot \Psi(X)^\top$ , and  $\widehat{C}^{11} = \Psi(Y) \cdot \Psi(Y)^\top$ . This way of approximating evolution operators using data is known as EDMD [6, 7].

The EDMD matrices can be used to extract approximate eigenfunctions of evolution operators by solving the eigenvalue problems

$$(\widehat{C}^{00})^+ \cdot \widehat{C}^{01} \cdot \xi = \lambda \cdot \xi, \quad (\widehat{C}^{11})^+ \cdot \widehat{C}^{10} \cdot \xi = \lambda \cdot \xi. \quad (5)$$

Given eigenvectors  $\xi_1, \dots, \xi_q$  corresponding to the leading eigenvalues  $\lambda_1, \dots, \lambda_q$  of (5), each vector encodes a linear combination of the basis functions. That is, for  $\psi: \mathbb{R}^d \rightarrow \mathbb{R}^n$  defined by  $\psi(x) = [\psi_1(x), \dots, \psi_n(x)]^\top$ , the  $k$ th eigenfunction is approximated by  $\tilde{\varphi}_k(x) = \xi_k^\top \psi(x)$ . In the self-adjoint case where  $\rho_0 = \rho_1 = \mu$  and  $\mathbb{V} = \mathbb{W}$ , it is readily shown that the eigenvalues  $\lambda_k$  of (5) satisfy the *variational principle* [8]

$$\sum_{k=1}^q \lambda_k = \sum_{k=1}^q \langle \mathcal{T}_\tau \tilde{\varphi}_k, \tilde{\varphi}_k \rangle_\mu \leq \sum_{k=1}^q \omega_k(\tau), \quad (6)$$

where  $\omega_k(\tau)$  are the leading eigenvalues of  $\mathcal{T}_\tau$ , provided they exist.

When considering a large number of basis functions, e.g., when  $n \gg m$ , storing the matrices  $\widehat{C}^{00}$ ,  $\widehat{C}^{01}$ ,  $\widehat{C}^{10}$ , and  $\widehat{C}^{11}$  or solving the resulting eigenvalue problem may be infeasible. However, if the trial spaces are identical,  $\mathbb{V} = \mathbb{W}$ , we can construct a reduced matrix such that the number of rows and columns is bounded by the number of snapshots  $m$ . This is known as *AMUSE (algorithm for multiple unknown signals extraction, cf. [33])*. In Algorithm 1, the method is formulated for the approximation of the Koopman operator, the case of the Perron-Frobenius operator is analogous. A proof of correctness of the algorithm and detailed derivations can be found in [5]. In Section 3, we will rewrite this algorithm in terms of low-rank tensor approximations.

**Algorithm 1: AMUSE for EDMD.**

---

**Input:** transformed data matrices  $\Psi(X)$  and  $\Psi(Y)$   
**Output:** solutions of (5) (approximation of the Koopman operator)

---

- 1: Compute a reduced SVD of  $\Psi(X)$ , i.e.,  $\Psi(X) = U \cdot \Sigma \cdot V^\top$ .
  - 2: Compute  $M = \Sigma^{-1} \cdot U^\top \cdot \Psi(X) \cdot \Psi(Y)^\top \cdot U \cdot \Sigma^{-1} = V^\top \cdot \Psi(Y)^\top \cdot U \cdot \Sigma^{-1}$ .
  - 3: Compute eigenvalues  $\lambda_k$  and right eigenvectors  $w_k$  of  $M$ .
  - 4: The eigenvectors are then given by  $\xi_k = U \cdot \Sigma^{-1} \cdot w_k$ .
- 

### 2.1.2 Forward-Backward Dynamics

For non-reversible or time-dependent systems, it is often more appropriate to approximate the *forward-backward operator*

$$\mathcal{F}_\tau = \mathcal{T}_\tau^* \mathcal{T}_\tau : L_{\rho_0}^2 \mapsto L_{\rho_0}^2,$$

since its leading eigenpairs can be used to calculate *finite-time coherent sets* [10, 11, 36, 13]. The data-based finite-dimensional approximation to  $\mathcal{F}_\tau$  is then given by  $F^\tau = (C^{00})^{-1} C^{01} (C^{11})^{-1} C^{10}$ , and coherent sets can be approximated based on eigenpairs of  $F^\tau$ :

$$F^\tau \xi = \lambda \xi. \quad (7)$$

Next, we show how the AMUSE algorithm can be adapted to obtain a reduced matrix eigenvalue problem for the discretized forward-backward operator  $F^\tau$ . The method, shown in Algorithm 2, is equivalent to canonical correlation analysis (CCA) [12, 13].

**Algorithm 2: AMUSE for CCA**

---

**Input:** transformed data matrices  $\Psi(X)$  and  $\Psi(Y)$   
**Output:** solutions of (7)

---

- 1: Compute reduced SVDs of  $\Psi(X)$  and  $\Psi(Y)$ , i.e.,  $\Psi(X) = U_X \cdot \Sigma_X \cdot V_X^\top$  and  $\Psi(Y) = U_Y \cdot \Sigma_Y \cdot V_Y^\top$ .
  - 2: Define  $M = \Sigma_Y^{-1} \cdot U_Y^\top \cdot \Psi(Y) \cdot \Psi(X)^\top \cdot U_X \cdot \Sigma_X^{-1} = V_Y^\top V_X$ .
  - 3: Compute singular values  $\sigma_k$  and right singular vectors  $w_k$  of  $M$ .
  - 4: The eigenvalues are given by  $\lambda_k = \sigma_k^2$ , and the eigenvectors are given by  $\xi_k = U_X \cdot \Sigma_X^{-1} \cdot w_k$ .
- 

**Lemma 1:** Solutions  $\lambda_k, w_k$  calculated by means of Algorithm 2 are solutions of (7) on subspaces  $\tilde{\mathbb{V}} \subset \mathbb{V}$  and  $\tilde{\mathbb{W}} \subset \mathbb{W}$ , defined by the columns of the transformations  $U_X \Sigma_X^{-1}$  and  $U_Y \Sigma_Y^{-1}$ .

*Proof.* Using the singular value decompositions of  $\Psi(X)$ , we find for the subspace  $\tilde{\mathbb{V}}$  that

$$\tilde{C}^{00} = [\Sigma_X^{-1} U_X^\top \Psi(X)] \cdot [\Psi(X)^\top U_X \Sigma_X] = \Sigma_X^{-1} U_X^\top U_X \Sigma_X^2 U_X^\top U_X \Sigma_X = \text{Id}.$$

We also have that  $\tilde{C}^{11} = \text{Id}$  by an analogous argument. It follows that the data-based approximation to  $\mathcal{F}^\tau$  on the subspaces  $\tilde{\mathbb{V}}$  and  $\tilde{\mathbb{W}}$  is given by

$$\begin{aligned} \tilde{F}^\tau &= \tilde{C}^{01} \tilde{C}^{10} = [\Sigma_X^{-1} U_X^\top \Psi(X)] [\Psi(Y)^\top U_Y \Sigma_Y^{-1}] \cdot [\Sigma_Y^{-1} U_Y^\top \Psi(Y)] [\Psi(X)^\top U_X \Sigma_X^{-1}] \\ &= (V_Y^\top V_X) \cdot (V_Y^\top V_X) = M^\top M. \end{aligned}$$

The statement follows from properties of the SVD of  $M$ . □

## 2.2 Low-rank tensor representations

Tensors are multi-dimensional arrays  $\mathbf{T} \in \mathbb{R}^N$ , where  $N = n_1 \times \dots \times n_p$ . Here,  $p$  is called the order of a tensor, while the dimensions of the elementary vector spaces (the so-called modes) are  $n_k, k = 1, \dots, p$ . Tensor entries are sometimes represented by multi-indices  $\mathbf{i} = (i_1, \dots, i_p)$  with  $i_k \in \{1, \dots, n_k\}$ , i.e.,  $\mathbf{T}_{\mathbf{i}} = \mathbf{T}_{i_1, \dots, i_p}$ . The single-index representation of the multi-index  $\mathbf{i}$  is denoted by  $\bar{\mathbf{i}} \in \{1, \dots, \prod_{k=1}^p n_k\}$ . Conversely, the multi-index representation of the single-index  $i \in \mathbb{N}$  is

represented by  $\dot{\iota}$ . The tensor product is denoted by  $\otimes$  and tensor multiplication/contraction by  $\cdot$ . We use bold capital letters ( $\mathbf{T}$ ,  $\mathbf{U}$ , etc.) to denote tensors, capital letters ( $U$ ,  $V$ , etc.) for matrices, and vectors and scalars are represented by lower case letters ( $x$ ,  $\alpha$ , etc.). For  $1 \leq k \leq p-1$ , the *mode- $k$  unfolding* of the tensor  $\mathbf{T}$  is the matrix

$$\mathbf{T} \begin{array}{c} | \\ n_{k+1}, \dots, n_p \\ | \\ \hline n_1, \dots, n_k \end{array} \in \mathbb{R}^{(n_1 \dots n_k) \times (n_{k+1} \dots n_p)}.$$

### 2.2.1 Tensor train format

We start by introducing the tensor train (TT) format, where a high-dimensional tensor is represented by the contraction of multiple low-dimensional tensors [20, 21].

**Definition 1:** A tensor  $\mathbf{T} \in \mathbb{R}^N$  is said to be in the TT format if

$$\mathbf{T} = \sum_{l_0=1}^{r_0} \dots \sum_{l_p=1}^{r_p} \bigotimes_{k=1}^p \mathbf{T}_{l_{k-1}, :, l_k}^{(k)} = \sum_{l_0=1}^{r_0} \dots \sum_{l_p=1}^{r_p} \mathbf{T}_{l_0, :, l_1}^{(1)} \otimes \dots \otimes \mathbf{T}_{l_{p-1}, :, l_p}^{(p)}.$$

The tensors  $\mathbf{T}^{(k)} \in \mathbb{R}^{r_{k-1} \times n_k \times r_k}$  of order 3 are called TT cores and the numbers  $r_k$  are called TT ranks. It holds that  $r_0 = r_p = 1$  and  $r_k \geq 1$  for  $k = 1, \dots, p-1$ .

The TT ranks  $r_0, \dots, r_p$  have a strong influence on the capability of representing a given tensor as a tensor train and determine the storage consumption of a tensor in the TT format. Figure 1 shows the graphical representation of a tensor train, which is also called Penrose notation, see [37].

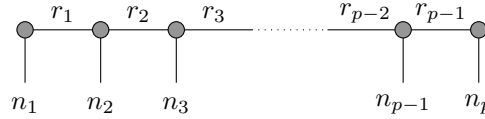


**Figure 1:** Graphical representation of a tensor train: A core is depicted by a circle with different arms indicating the modes of the tensor and the rank indices. The first and the last TT core are regarded as matrices due to the fact that  $r_0 = r_p = 1$ .

We also represent TT cores as two-dimensional arrays containing vectors as elements. For a given tensor train  $\mathbf{T} \in \mathbb{R}^N$  with cores  $\mathbf{T}^{(k)} \in \mathbb{R}^{r_{k-1} \times n_k \times r_k}$ , a single core is written as

$$\llbracket \mathbf{T}^{(k)} \rrbracket = \begin{bmatrix} \mathbf{T}_{1, :, 1}^{(k)} & \dots & \mathbf{T}_{1, :, r_k}^{(k)} \\ \vdots & \ddots & \vdots \\ \mathbf{T}_{r_{k-1}, :, 1}^{(k)} & \dots & \mathbf{T}_{r_{k-1}, :, r_k}^{(k)} \end{bmatrix}.$$

We then use the notation  $\mathbf{T} = \llbracket \mathbf{T}^{(1)} \rrbracket \otimes \dots \otimes \llbracket \mathbf{T}^{(p)} \rrbracket$  for representing tensor trains  $\mathbf{T}$ , cf. [24, 26, 38]. This notation can be regarded as a generalization of the standard matrix multiplication. The difference is that we here compute the tensor products of the corresponding elements – which are vectors instead of scalar values – and then sum over the columns and rows, respectively. A core of a tensor train is *left-orthonormal* if

$$\left( \mathbf{T}^{(k)} \begin{array}{c} | \\ r_k \\ | \\ r_{k-1}, n_k \end{array} \right)^\top \cdot \left( \mathbf{T}^{(k)} \begin{array}{c} | \\ r_k \\ | \\ r_{k-1}, n_k \end{array} \right) = \text{Id} \in \mathbb{R}^{r_k \times r_k}.$$

### 2.2.2 Global SVD and pseudoinverse

Given a tensor train  $\mathbf{T}$  of order  $p+1$ , we will require an SVD of its mode- $p$  unfolding. A method to accomplish this goal was presented in [34]. The method provides a tensor train in form of

a segment  $\mathbf{U} \in \mathbb{R}^{n_1 \times \dots \times n_p \times r}$ , a diagonal coupling matrix  $\Sigma \in \mathbb{R}^{r \times r}$ , and an orthonormal  $V \in \mathbb{R}^{n_{p+1} \times r}$  representing the last core. The dimension  $r$  is the TT rank between the two last cores. Just like a standard SVD of a matrix,  $\mathbf{U}$ ,  $\Sigma$ , and  $V$  then satisfy the following properties:

- i)  $\mathbf{T} = \mathbf{U} \cdot \Sigma \cdot V^\top$ ,
- ii)  $\mathbf{U}^\top \cdot \mathbf{U} = V^\top \cdot V = \text{Id} \in \mathbb{R}^{r \times r}$ ,
- iii)  $\Sigma \in \mathbb{R}^{r \times r}$  is a diagonal matrix.

### 2.2.3 Basis Decompositions

Within the context of data-driven approximation of evolution operators, see Section 2.1, tensors arise if trial spaces are chosen as tensor products of elementary function spaces. We consider a data matrix  $X \in \mathbb{R}^{d \times m}$  originating from a stochastic process  $\mathcal{X}_t$ , and a set of basis functions  $\psi_1, \dots, \psi_p$  with  $\psi_k: \mathbb{R}^d \rightarrow \mathbb{R}^{n_k}$  where  $n_k \in \mathbb{N}$  for  $k = 1, \dots, p$ . Let  $\mathbb{V}^k = \text{span}\{\psi_{k,1}, \dots, \psi_{k,n_k}\}$  denote the  $n_k$ -dimensional subspaces spanned by the elementary basis functions  $\psi_{k,1}, \dots, \psi_{k,n_k} \in L^2_{\rho_0}$ . We consider the Galerkin projection (3) on the tensor product  $\mathbb{V} := \mathbb{V}^1 \otimes \dots \otimes \mathbb{V}^p \subset L^2_{\rho_0}$ , which is a subspace of dimension at most  $n_1 \cdot \dots \cdot n_p$ . Equivalently, choosing elementary basis functions in  $L^2_{\rho_1}$  for a data matrix  $Y$  yields a tensor space  $\mathbb{W} \subset L^2_{\rho_1}$ .

The tensor-based counterparts of the transformed data matrices given in (4) are denoted by  $\Psi(X)$  and  $\Psi(Y)$ , respectively. These *transformed data tensors* can then be used to obtain empirical estimates of  $C^{01}$  and  $C^{00}$ , i.e.,  $\widehat{C}^{01} = \Psi(X) \cdot \Psi(Y)^\top$  and  $\widehat{C}^{00} = \Psi(X) \cdot \Psi(X)^\top$ , and to solve the resulting eigenvalue problem as described in (5). As we have shown in [26], the tensor train format can be used to represent transformed data tensors. In what follows, we will focus on the construction of  $\Psi(X)$ , the case for  $\Psi(Y)$  is analogous. That is, we consider the rank-one tensors of the form

$$\Psi(x) = \psi_1(x) \otimes \dots \otimes \psi_p(x) = \begin{bmatrix} \psi_{1,1}(x) \\ \vdots \\ \psi_{1,n_1}(x) \end{bmatrix} \otimes \dots \otimes \begin{bmatrix} \psi_{p,1}(x) \\ \vdots \\ \psi_{p,n_p}(x) \end{bmatrix} \in \mathbb{R}^{n_1 \times n_2 \times \dots \times n_p}. \quad (8)$$

Note that the so-called *coordinate-major* and *function-major* basis decompositions, introduced in [26], are special cases of the more general decomposition given in (8). The transformed data tensor  $\Psi(X) \in \mathbb{R}^{n_1 \times \dots \times n_p \times m}$  is then given by adding the rank-one decompositions (8) for all vectors  $x_1, \dots, x_m$  and taking the tensor product with an additional unit vector. The result is the following TT decomposition:

$$\begin{aligned} \Psi(X) &= \sum_{k=1}^m \Psi(x_k) \otimes e_k \\ &= \sum_{k=1}^m \psi_1(x_k) \otimes \dots \otimes \psi_p(x_k) \otimes e_k \\ &= \begin{bmatrix} \psi_1(x_1) & \dots & \psi_1(x_m) \end{bmatrix} \otimes \begin{bmatrix} \psi_2(x_1) & & 0 \\ & \ddots & \\ 0 & & \psi_2(x_m) \end{bmatrix} \otimes \dots \\ &\quad \dots \otimes \begin{bmatrix} \psi_p(x_1) & & 0 \\ & \ddots & \\ 0 & & \psi_p(x_m) \end{bmatrix} \otimes \begin{bmatrix} e_1 \\ \vdots \\ e_m \end{bmatrix} \\ &=: \left[ \Psi^{(1)}(X) \right] \otimes \left[ \Psi^{(2)}(X) \right] \otimes \dots \otimes \left[ \Psi^{(p)}(X) \right] \otimes \left[ \Psi^{(p+1)}(X) \right], \end{aligned} \quad (9)$$

where  $e_k$ ,  $k = 1, \dots, m$ , denote the unit vectors of the standard basis in the  $m$ -dimensional Euclidean space. The matrix-based counterpart of  $\Psi(X)$ , see (4), would be given by the mode- $p$  unfolding

$$\Psi(X) = \Psi(X) \Big|_{n_1, \dots, n_p}^m, \quad (10)$$



that is, modes  $n_1, \dots, n_p$  represent row indices of the unfolding, and mode  $m$  is the column index.

## 2.2.4 Higher-order CUR decomposition

For a matrix  $M \in \mathbb{R}^{m \times n}$ , a CUR decomposition consists of index sets  $I, J$ , as well as submatrices  $C = M_{:,J}$ ,  $U = M_{I,J}$ , and  $R = M_{I,:}$ , such that  $M \approx C \cdot U^{-1} \cdot R$ , see Figure 2.

$$\begin{bmatrix} \cdot & \cdot & \cdot & \cdot & \cdot & \cdot \\ \cdot & \cdot & \cdot & \cdot & \cdot & \cdot \\ \cdot & \cdot & \cdot & \cdot & \cdot & \cdot \\ \cdot & \cdot & \cdot & \cdot & \cdot & \cdot \\ \cdot & \cdot & \cdot & \cdot & \cdot & \cdot \\ \cdot & \cdot & \cdot & \cdot & \cdot & \cdot \end{bmatrix} \approx \begin{bmatrix} | & | & | & | \\ | & | & | & | \\ | & | & | & | \\ | & | & | & | \end{bmatrix} \cdot \begin{bmatrix} \times & \times & \times \\ \times & \times & \times \\ \times & \times & \times \end{bmatrix}^{-1} \cdot \begin{bmatrix} \text{---} \\ \text{---} \\ \text{---} \end{bmatrix}$$

**Figure 2:** CUR decomposition: The matrix on the left-hand side is approximated by the matrix product  $C \cdot U^{-1} \cdot R$ , where  $C$  (blue lines) is a column subset,  $R$  (green lines) is a row subset, and  $U$  (red crosses) is the intersection matrix.

There are different methods to find optimal sets of rows and columns, cf. [39]. An important subproblem is the following: given a set of column indices  $J = \{j_1, \dots, j_r\}$  with  $r \leq \min(m, n)$  (and  $M_{:,J}$  having full column rank), find an optimal subset of row indices  $I = \{i_1, \dots, i_r\}$ . This problem can be solved by applying the *maximum-volume principle* to  $M_{:,J}$ , so that the infinity norm of  $M - M_{:,J} \cdot M_{I,J}^{-1} \cdot M_{I,:}$  is minimized over  $I$ , see [40, 41]. We refer to this algorithm as *Maxvol* from now on.

As described in [35], the CUR decomposition can be generalized to a tensor if its mode- $k$  unfoldings are successively decomposed using CURs. This method presents an alternative to the decomposition (9) if applied to the transformed data tensor  $\Psi(X)$ . However, the procedure requires pre-defined row and column subsets for each unfolding. The authors of [35] also suggested a greedy algorithm to circumvent this problem: after initializing row and column subsets in some way, the method alternates between updating the column subsets while all row sets are fixed, and vice versa. This algorithm is the basis of the method we present in Sec. 3.1.

## 3 AMUSE on tensors

In what follows, we present different methods which enable us to solve tensorized versions of the eigenvalue problems (5) and (7). First, we present an alternative construction of TT representations for transformed data tensors based on the HOCUR decomposition discussed in Section 2.2.4. Afterwards, we will derive the tensor-based counterparts of AMUSE corresponding to EDMD as well as CCA. Henceforth, the resulting tensor-based methods will be called *AMUSEt* (*AMUSE on tensors*).

### 3.1 HOCUR for transformed data tensors

In practice, the direct construction of transformed data tensors as described in Section 2.2.3 may be infeasible due to a large number of basis functions or snapshots. Our idea to circumvent this problem is a combination of different techniques from [35, 40, 41], specifically adapted to transformed data tensors as described in Section 2.2.3. As suggested in [35], Algorithm 3 successively updates the rows sets of the unfolded residual tensors during a forward loop, while all column sets are fixed. Then, column sets are updated during a backward loop, with all row sets fixed, and the entire procedure is repeated until convergence. The key insight, used in lines 5 – 9 and 13 – 14, is that each update only operates on a small subtensor which is easily evaluated. Assume we are given a row set  $\mathbf{I} = \mathbf{I}_q = \{\mathbf{i}_1, \dots, \mathbf{i}_{r_q}\}$  of multi-indices comprising modes  $n_1, \dots, n_q$ , and a column set  $\mathbf{J} = \mathbf{J}_{q+2} = \{\mathbf{j}_1, \dots, \mathbf{j}_s\}$  of multi-indices comprising modes  $n_{q+2}, \dots, n_p, m$ :

$$\begin{aligned} \mathbf{i}_1, \dots, \mathbf{i}_{r_q} &\in \{1, \dots, n_1\} \times \dots \times \{1, \dots, n_q\}, \\ \mathbf{j}_1, \dots, \mathbf{j}_s &\in \{1, \dots, n_{q+2}\} \times \dots \times \{1, \dots, n_p\} \times \{1, \dots, m\}. \end{aligned}$$

Then, a new extended row set comprising the first  $q + 1$  modes

$$\mathbf{i}_1, \dots, \mathbf{i}_{r_{q+1}} \in \{1, \dots, n_1\} \times \dots \times \{1, \dots, n_{q+1}\},$$

can be obtained by applying Algorithm Maxvol to the submatrix  $\Psi(X)_{|\mathbf{I}, \mathbf{J}} \in \mathbb{R}^{r_q \cdot n_{q+1} \times s}$ , given by

$$\Psi(X)_{|\mathbf{I}, \mathbf{J}} = \begin{bmatrix} \Psi(X)_{\mathbf{i}_1, :; \mathbf{j}_1} & \cdots & \Psi(X)_{\mathbf{i}_1, :; \mathbf{j}_s} \\ \vdots & \ddots & \vdots \\ \Psi(X)_{\mathbf{i}_{r_q}, :; \mathbf{j}_1} & \cdots & \Psi(X)_{\mathbf{i}_{r_q}, :; \mathbf{j}_s} \end{bmatrix}. \quad (11)$$

This matrix is easily set up using basis function evaluations. More precisely, given multi-indices  $\mathbf{i} = (i_1, \dots, i_q) \in \mathbf{I}$  and  $\mathbf{j} = (j_{q+2}, \dots, j_p, k) \in \mathbf{J}$ , entries  $\Psi(X)_{\mathbf{i}, :; \mathbf{j}}$  of  $\Psi(X)_{|\mathbf{I}, \mathbf{J}}$  are given by

$$\begin{aligned} \Psi(X)_{\mathbf{i}, :; \mathbf{j}} &= \Psi(X)_{i_1, \dots, i_q, :; i_{q+2}, \dots, i_p, k} \\ &= \underbrace{\psi_{1, i_1}(x_k) \cdot \dots \cdot \psi_{q, i_q}(x_k)}_{\in \mathbb{R}} \cdot \underbrace{\psi_{q+1}(x_k)}_{\in \mathbb{R}^{n_{q+1}}} \cdot \underbrace{\psi_{q+2, i_{q+2}}(x_k) \cdot \dots \cdot \psi_{p, i_p}(x_k)}_{\in \mathbb{R}}. \end{aligned}$$

Note that the last entry of the column index  $\mathbf{j}$  determines the snapshot  $x_k$  where the product is evaluated.

**Algorithm 3: Higher-order CUR decomposition.**

---

**Input:** data matrix  $X = [x_1, \dots, x_m] \in \mathbb{R}^{d \times m}$ , basis functions  $\psi_{i, j_i}$ ,  $i = 1, \dots, p$ ,  $j_i = 1, \dots, n_i$ , maximum ranks  $r_1, \dots, r_p$  with  $r_q \leq n_{q+1} \cdot r_{q+1}$ , number of iterations  $N$ , multiplier  $\alpha > 1$

**Output:** TT approximation of the transformed data tensor  $\Psi(X)$

---

- 1: Set  $n_{p+1} = m$ ,  $r_0 = r_{p+1} = 1$ , and  $\mathbf{I}_0 = \{\emptyset\}$ .
  - 2: Define initial multi-index column sets  $\mathbf{J}_2, \dots, \mathbf{J}_{p+2}$ .
  - 3: **for**  $k = 1, \dots, N$  **do**
  - 4:   **for**  $l = 1, \dots, p$  **do** (First half sweep)
  - 5:     Extract submatrix  $M = \Psi(X)_{|\mathbf{I}_{l-1}, \mathbf{J}_{l+1}}$ , see (11).
  - 6:     **if**  $k = 1$  **then**
  - 7:       Find set of linearly independent columns  $J$  of  $M$  with  $|J| \leq r_l$ .
  - 8:       Set  $M$  to  $M_{:, J}$  and  $r_l$  to  $|J|$ .
  - 9:     Apply Algorithm Maxvol to  $M$  to extract row set  $I$ .
  - 10:     Compute multi-index row set  $\mathbf{I}_l$  from  $\mathbf{I}_{l-1}$  and  $I$ , see (12).
  - 11:     Define core  $\Psi(X)^{(l)}$  as  $M \cdot M_{I, :}^{-1}$  reshaped as  $\mathbb{R}^{r_{l-1} \times n_l \times r_l}$ .
  - 12:   **for**  $l = p + 1, \dots, 2$  **do** (Second half sweep)
  - 13:     Extract submatrix  $M = \Psi(X)_{|\mathbf{I}_{l-1}, \mathbf{J}_{l+1}}$  and reshape as  $\mathbb{R}^{r_{l-1} \times n_l \cdot r_l}$ .
  - 14:     Apply Algorithm Maxvol to  $M^T$  to extract column set  $J$  and set  $r_{l-1} = |J|$ .
  - 15:     Compute multi-index column set  $\mathbf{J}_l$  from  $J$  and  $\mathbf{J}_{l+1}$ .
  - 16:     Define core  $\Psi(X)^{(l)}$  as  $M_{:, J}^{-1} \cdot M$  reshaped as  $\mathbb{R}^{r_{l-1} \times n_l \times r_l}$ .
  - 17: Define first core  $\Psi(X)^{(1)}$  as  $\Psi(X)_{|\mathbf{I}_0, \mathbf{J}_2}$  reshaped as  $\mathbb{R}^{1 \times n_1 \times r_1}$ .
- 

Let us elaborate on a few more details of Algorithm 3. First, note that multi-index sets for the construction of the submatrices  $\Psi(X)_{|\mathbf{I}, \mathbf{J}}$  are nested sets by construction. In Line 10, after each application of Algorithm Maxvol, the resulting single-index set  $I = \{i_1, \dots, i_{r_{q+1}}\}$  needs to be converted into a multi-index row set for modes  $n_1, \dots, n_{q+1}$ . Given a multi-index row set  $\mathbf{I}_q = \{\mathbf{i}_1, \dots, \mathbf{i}_{r_q}\}$  as above, each row of  $\Psi(X)_{|\mathbf{I}_q, \mathbf{J}_{q+2}}$  can naturally be associated with a multi-index  $(k_1, k_2) \in \{1, \dots, r_q\} \times \{1, \dots, n_{q+1}\}$ . Hence, we map each single-index  $i_k \in I$  to a multi-index  $\hat{i}_k = (\hat{i}_{k,1}, \hat{i}_{k,2})$  in  $\{1, \dots, r_q\} \times \{1, \dots, n_{q+1}\}$ , and then define the extended multi-index row set

$$\mathbf{I}_{q+1} = \{(\hat{i}_{1,1}, \hat{i}_{1,2}), \dots, (\hat{i}_{r_{q+1},1}, \hat{i}_{r_{q+1},2})\}. \quad (12)$$

Column sets are updated analogously in Line 15 of Algorithm 3.



Second, the algorithm requires initial column sets which are generated in Line 2. While it was suggested in [35] to pick these columns at random, we build them up recursively to ensure the column sets are also nested. Starting from  $\mathbf{J}_{p+2} = \{\emptyset\}$ , column set  $\mathbf{J}_q$  is obtained by simply selecting the first  $\min(\alpha \cdot r_q, n_{q+1} \cdot r_{q+1})$  indices out of the index set  $\{1, \dots, n_{q+1} \cdot r_{q+1}\}$ , and then joining them with multi-index column set  $\mathbf{J}_{q+1}$  as described above in (12). In practice, we found it helpful to select a rather large number of columns at this point, as these initial columns would often be highly redundant. The parameter  $\alpha$  can be tuned to ensure enough columns are selected during the initialization stage.

Third, we need to find index sets of linearly independent columns of the matrices  $\Psi(X)_{\mathbf{I}, \mathbf{J}}$  during the first iteration, see Line 7. This can again be done by applying QR decompositions with column pivoting. And finally, the cores of the TT approximation of  $\Psi(X)$  are updated in Lines 11 and 16, by multiplication of parts of the determined CUR decomposition. In the notation used in Section 2.2.4, the updated cores are given by tensor foldings of  $C \cdot U^{-1}$  and  $U^{-1} \cdot R$ , respectively.

### 3.2 AMUSEt for tensor-based EDMD

Given a TT representation of the transformed data tensors  $\Psi(X)$ ,  $\Psi(Y)$ , e.g., by (9) or by application of Algorithm 3, we now discuss the solution of the eigenvalue problem (5) with empirical estimates

$$\hat{C}^{01} = \Psi(X) \cdot \Psi(Y)^\top \quad \text{and} \quad \hat{C}^{00} = \Psi(X) \cdot \Psi(X)^\top.$$

Instead of solving this eigenvalue problem in the TT format, cf. [24, 42], we use a tensor-based counterpart of the AMUSE algorithm discussed in Section 2.1 by constructing a reduced eigenvalue problem with the same spectrum as (5). The basic idea of AMUSEt for tensor-based EDMD is to first compute a global SVD of  $\Psi(X)$ , i.e.  $\Psi(X) = \mathbf{U} \cdot \Sigma \cdot V^\top$ , and then to construct the reduced matrix  $M$  as in Line 2 of Algorithm 1, which leads to the contraction of the tensor network shown in Figure 3.

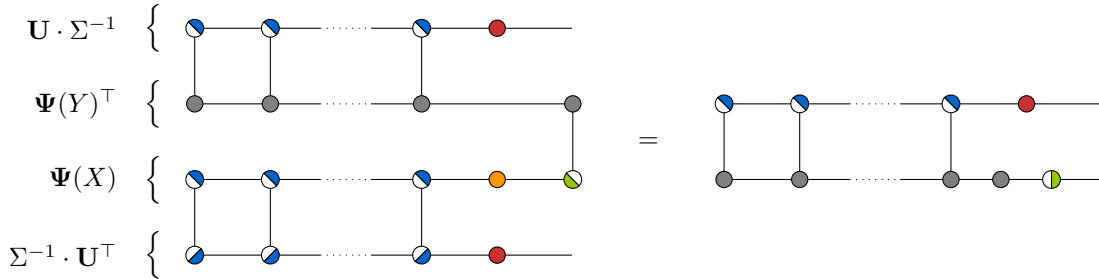


**Figure 3:** Graphical representation of the reduced matrix: Given  $\Psi(X)$  (in form of a global SVD) and  $\Psi(Y)$ , the reduced matrix  $M \in \mathbb{R}^{r \times r}$  is computed by contracting the above tensor network. Half-filled circles in blue depict the cores of  $\mathbf{U}$ ,  $\Sigma$  and  $\Sigma^{-1}$  are represented by orange and red circles, respectively, and the half-filled circle in green depicts the matrix  $V$  of the global SVD. Since we here do not assume any further properties on  $\Psi(Y)$ , we simply represent its TT cores by gray circles.

However, the complexity of AMUSEt for tensor-based EDMD can be reduced further in many cases. Oftentimes, we consider snapshot matrices  $X, Y \in \mathbb{R}^{d \times m}$ , which are extracted from a trajectory data matrix  $Z \in \mathbb{R}^{d \times \tilde{m}}$ ,  $\tilde{m} > m$ , and share a large number of common snapshot vectors. Instead of constructing the transformed data tensors separately, we can construct the TT decomposition of  $\Psi(Z)$  and then simply restrict the last TT core to the respective time steps in order to obtain the representations for  $\Psi(X)$  and  $\Psi(Y)$ . That is, given the data matrix  $Z$ , and index sets  $I_X, I_Y$  such that  $X = Z_{:, I_X}$  and  $Y = Z_{:, I_Y}$ , we construct

$$\Psi(Z) = \left[ \Psi^{(1)}(Z) \right] \otimes \left[ \Psi^{(2)}(Z) \right] \otimes \dots \otimes \left[ \Psi^{(p)}(Z) \right] \otimes \left[ \Psi^{(p+1)}(Z) \right]$$

either by the direct approach, see Section 2.2.3, or by applying Algorithm 3. Then, the tensor

tensors  $\Psi(X)$  and  $\Psi(Y)$  are given by

$$\Psi(X) = \left[ \left[ \Psi^{(1)}(Z) \right] \otimes \left[ \Psi^{(2)}(Z) \right] \otimes \dots \otimes \left[ \Psi^{(p)}(Z) \right] \otimes \left[ \left( \Psi^{(p+1)}(Z) \right)_{:,I_X,1} \right] \right]$$

and

$$\Psi(Y) = \left[ \left[ \Psi^{(1)}(Z) \right] \otimes \left[ \Psi^{(2)}(Z) \right] \otimes \dots \otimes \left[ \Psi^{(p)}(Z) \right] \otimes \left[ \left( \Psi^{(p+1)}(Z) \right)_{:,I_Y,1} \right] \right].$$

Hence, we first left-orthonormalize the tensor train  $\Psi(Z)$  and then extract  $\Psi(X)$  as well as  $\Psi(Y)$  by restricting the last core to the corresponding indices.

**Remark 1:** Even if the matrices  $X, Y \in \mathbb{R}^{d \times m}$  are not extracted from a single trajectory matrix, we can still define  $Z := [X, Y]$  as well as  $I_X = \{1, \dots, m\}$ ,  $I_Y = \{m+1, \dots, 2m\}$  and apply the orthonormalization method described above.

Additionally, we construct a global SVD of  $\Psi(X)$  in the form of  $\mathbf{U} \cdot U_X \cdot \Sigma_X \cdot V_X^\top$ . That is, we compute an SVD of the last core of  $\Psi(X)$  after left-orthonormalization. The respective transformations of the considered tensor trains are visualized in Figure 4.

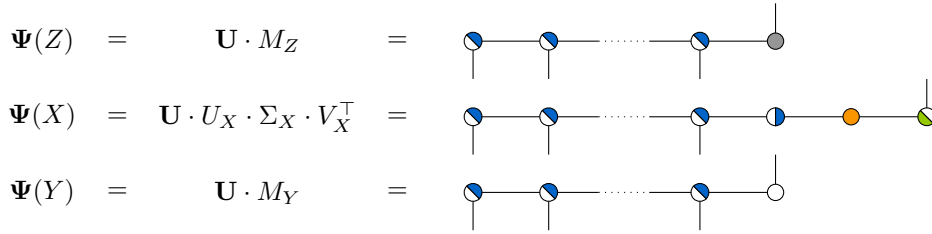


**Figure 4:** Construction of transformed data tensors: The tensor trains  $\Psi(X)$  and  $\Psi(Y)$  are extracted from the left-orthonormalized tensor train  $\Psi(Z)$ . Additionally,  $\Psi(X)$  is represented by its global SVD. Again, the cores of  $\mathbf{U}$  (as well as  $U_X$ ) are represented by half-filled circles in blue,  $\Sigma_X$  by an orange circle, and  $V_X$  by a half-filled green circle. The last cores of  $\Psi(Z)$  and  $\Psi(Y)$  are depicted by a gray and a white circle, respectively. Here, we transpose the last TT core in order to account for the different row and column dimensions of the transformed data matrices, cf. Section 2.2.3.

By construction,  $\Psi(X)$  and  $\Psi(Y)$  share the same segment  $\mathbf{U}$ . Since the cores of  $\mathbf{U}$  (as well as  $U_X$ ) are left-orthonormal, most of the contractions cancel out, and only four matrices remain, namely  $V_X^\top$ ,  $M_Y$ ,  $U_X$ , and  $\Sigma_X^{-1}$ . Thus, the reduced matrix is then simply given by

$$M = \Sigma_X^{-1} \cdot U_X^\top \cdot \mathbf{U}^\top \cdot \Psi(X) \cdot \Psi(Y)^\top \cdot \mathbf{U} \cdot U_X \cdot \Sigma_X^{-1} = V_X^\top \cdot M_Y^\top \cdot U_X \cdot \Sigma_X^{-1}. \quad (13)$$

Furthermore, we are typically not interested in the full eigentensors but rather in the projections of the data onto approximate eigenfunctions of the Koopman operator (1). Given the  $q$  leading eigenvectors of the reduced matrix  $M$  in form of a matrix  $W = [w_1, \dots, w_q]$ , the eigentensors of  $(\hat{\mathbf{C}}^{00})^+ \cdot \hat{\mathbf{C}}^{01}$  can be expressed as a tensor train  $\Xi$  with  $\Xi = \mathbf{U} \cdot U_X \cdot \Sigma_X^{-1} \cdot W$ , see Line 4 of Algorithm 1. The evaluations of the associated eigenfunctions at all snapshots are then given by the matrix  $\Phi = \Xi^\top \cdot \Psi(X)$ , see [5]. The corresponding tensor network also breaks down to a simple matrix product, as is shown in Figure 5.

**Remark 2:** Note that we do not need the cores of  $\mathbf{U}$  after the orthonormalization procedure if we are only interested in the approximated eigenfunctions. For both the construction of the reduced matrix  $M$  (Figure 3) as well as the eigenfunction evaluations  $\Phi$  (Figure 5), the TT segment  $\mathbf{U}$  is not required due to its orthonormality. In particular, when using the HOSVD approach, this significantly reduces the storage consumption since we are able to construct the left-orthonormalized version of  $\Psi(X)$  step by step, i.e., we only need to store two TT cores in memory at the same time.

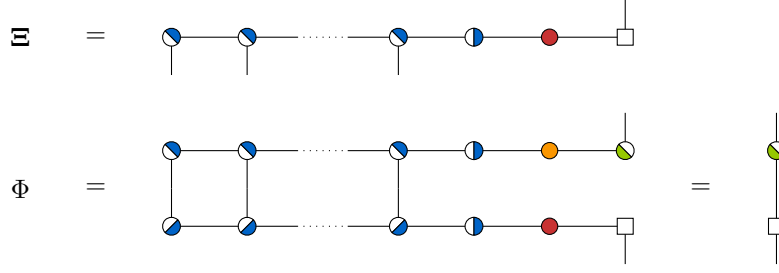


**Figure 5:** Graphical representation of the eigentensors and eigenfunctions: The tensor train  $\Xi$  is built by the contraction of  $\mathbf{U}$ ,  $U_X$ ,  $\Sigma^{-1}$ , and  $W$  (depicted by the square). The matrix  $\Phi$  comprising the evaluations of the eigenfunctions at the given snapshots is constructed by multiplying the tensors  $\Psi(X)$  and  $\Xi$ . Similar to the construction of the reduced matrix, see Figure 3, only a few cores remain since the orthonormal cores cancel out and  $\Sigma$  is multiplied by its inverse.

### 3.3 AMUSEt for tensor-based CCA

The tensor networks corresponding to AMUSEt for tensor-based CCA are similar to the ones described in the previous section. Again, we construct the transformed data tensors  $\Psi(X)$  and  $\Psi(Y)$  as explained in Section 2.2.3. However, here we do not apply a simultaneous left-orthonormalization of these tensors, instead we compute global SVDs of  $\Psi(X)$  and  $\Psi(Y)$  separately, cf. Section 2.2.2. That is, the reduced matrix  $M$  for the tensor-based counterpart of Algorithm 2 is simply given by the contraction of the last TT cores of the global SVDs of  $\Psi(X)$  and  $\Psi(Y)$ . Analogous to AMUSEt for tensor-based EDMD, the evaluation of eigenfunctions of the forward-backward operator at snapshots given in the matrix  $X$  leads to the multiplication of the right singular vectors of  $M$  by the last TT core of the global SVD of  $\Psi(X)$ , see Figure 5.

### 3.4 Subspace interpretation

The goal of this section is to provide an initial convergence analysis of the methods introduced above. We focus on the case where data tensors  $\Psi(X)$  and  $\Psi(Y)$  are given in the form (9). We start by showing that computing the global SVD of  $\Psi(X)$  in this form amounts to selecting an  $r_p$ -dimensional subspace of the full tensor space  $\mathbb{V}$ . In this section, we will denote all quantities derived from data by a  $\hat{\cdot}$  in order to distinguish those from their analytical counterparts.

**Lemma 2:** After  $k$  steps of the global SVD algorithm applied to the decomposition (9), core  $\Psi^{(k+1)}(X)$ , viewed as a matrix in  $\mathbb{R}^{r_k \cdot n_{k+1} \times m}$ , contains the time series of  $r_k \cdot n_{k+1}$  functions of the form

$$\hat{\eta}_{k,l_k}(x) \cdot \psi_{k+1,i_{k+1}}(x), \quad l_k = 1, \dots, r_k, \quad i_{k+1} = 1, \dots, n_{k+1},$$

with  $\hat{\eta}_{k,l_k} \in \bigotimes_{l=1}^k \mathbb{V}^l$  and  $\psi_{k+1,i_{k+1}} \in \mathbb{V}^{k+1}$ .

*Proof.* The statement clearly holds for  $k = 0$  with  $\hat{\eta}_{0,1} = 1$ , so let us consider a general  $k$  and assume it is true for all cores up to  $\Psi^{(k)}(X)$ . Consider the singular value decomposition  $\Psi^{(k)}(X) = \hat{U}_k \cdot \hat{\Sigma}_k \cdot \hat{V}_k^\top$ . The columns of  $\hat{U}_k$  encode  $r_k$  linear combinations of the functions represented by  $\Psi^{(k)}(X)$ , denote those functions by  $\hat{\eta}_{k,l_k} \in \bigotimes_{l=1}^k \mathbb{V}^l$  for  $l_k = 1, \dots, r_k$ . The time series of these functions along the data are given by  $\hat{U}_k^\top \cdot \Psi^{(k)}(X) = \hat{\Sigma}_k \cdot \hat{V}_k^\top \in \mathbb{R}^{r_k \times m}$ . The scaled right singular vectors thus provide the time series of the basis functions selected during the  $k$ th compression step. After contracting  $\hat{\Sigma}_k \cdot \hat{V}_k^\top$  and the next core, the updated core  $\Psi^{(k+1)}(X)$  becomes

$$\begin{aligned} \Psi^{(k+1)}(X)_{l_k, i_{k+1}, t} &= \sum_{t'=1}^m \left[ \hat{\Sigma}_k \hat{V}_k^\top \right]_{l_k, t'} \cdot \delta_{t, t'} \cdot \psi_{k+1, i_{k+1}}(x_t) \\ &= \hat{\eta}_{k, l_k}(x_t) \cdot \psi_{k+1, i_{k+1}}(x_t). \end{aligned} \quad \square$$

Applying this argument  $p$  times, it follows that the global left singular vectors  $\hat{U}$  in Section 2.2.2 encode an  $r_p$ -dimensional subspace of the full tensor space  $\mathbb{V}$ , and the tensor  $\hat{U} \cdot \hat{\Sigma}^{-1}$  provides

a corresponding orthonormal basis. For fixed ranks  $r_1, \dots, r_p$  and given some technical assumptions, we will show below that this transformation converges in the limit of infinite data. We start by making the following recursive definition:

**Definition 2:** Let  $\mathbb{F}^0 = \text{span}\{1\}$ . For  $1 \leq k \leq d$ , we first define  $\mathbb{U}^k := \mathbb{F}^{k-1} \otimes \mathbb{V}^k$ . Then, we define  $\mathbb{F}^k$  as the subspace of functions in  $\mathbb{U}^k$  encoded by the matrix of leading  $r_k$  eigenvectors of the Galerkin matrix  $C_{\mathbb{U}^k}^{00}$ . The corresponding data-driven subspaces are denoted by  $\hat{\mathbb{U}}^k$  and  $\hat{\mathbb{F}}^k$ . We also define  $\mathbb{S}^k$  by

$$\mathbb{S}^k = \bigotimes_{l=1}^k \mathbb{V}^l.$$

We will also need the notion of distance between subspaces in Euclidean space. Let  $\mathbb{F}, \mathbb{G} \subset \mathbb{R}^q$  be subspaces. Their distance  $d(\mathbb{F}, \mathbb{G})$  is then defined by the largest approximation error by vectors in  $\mathbb{G}$  for all unit vectors in  $\mathbb{F}$ , see for example [43][Ch. II.4]:

$$d(\mathbb{F}, \mathbb{G}) := \sup_{x \in \mathbb{F}, \|x\|=1} \inf_{y \in \mathbb{G}} \|x - y\|.$$

**Proposition 1:** Consider the global SVD algorithm applied to (9) at fixed ranks  $r_k, k = 1, \dots, p$ . Moreover, assume that the Galerkin matrices  $C_{\mathbb{U}^k}^{00}$  possess a positive singular value gap between their  $(r_k)$ -th and  $(r_{k+1})$ -th singular value. Then, the subspace represented by  $\hat{\mathbb{U}}$  converges to  $\mathbb{F}^p$  for infinite data size.

*Proof.* For each  $1 \leq k \leq p$ , the spaces  $\mathbb{F}^k$  and  $\hat{\mathbb{F}}^k$  are subspaces of  $\mathbb{S}^k$ . Hence, we will measure their distances by identifying them with the corresponding subspaces  $\mathbb{G}^k, \hat{\mathbb{G}}^k$  of  $\mathbb{R}^{n_1 \dots n_k}$ , and then considering the distance  $d(\mathbb{G}^k, \hat{\mathbb{G}}^k)$  between subspaces in Euclidean space. We will show by induction that for a sufficient amount of data, the distance  $d(\mathbb{G}^p, \hat{\mathbb{G}}^p)$  can be made arbitrarily small with high probability. We fix an error tolerance  $\epsilon$  and a confidence level  $\alpha = 1 - 2^{-j}$  for  $j \geq 1$ . Denoting the singular value gaps of the  $C_{\mathbb{U}^k}^{00}$  by  $\delta_k > 0$ , we introduce the following constants

$$\delta := \max_{k=1, \dots, p} \delta_k, \quad \beta := 2 \max_{k=1, \dots, p} \|C_{\mathbb{S}^k}^{00}\|_2.$$

Step 1: By ergodicity of the process, we can find an  $m_1 \in \mathbb{N}$  such that, if  $m \geq m_1$ , we have that

$$\|\hat{C}_{\mathbb{V}^1}^{00} - C_{\mathbb{V}^1}^{00}\|_2 \leq \frac{\epsilon \delta}{2^{p-1}(2\beta\delta^{-1} + 1)^{p-1}}$$

with probability at least  $1 - 2^{-(j+2(p-1))}$ . It follows from the Davis–Kahan theorem, see, e.g., [43, Ch. 5, Thm. 3.6], that with at least the same probability

$$d(\mathbb{G}^1, \hat{\mathbb{G}}^1) \leq \frac{\epsilon}{2^{p-1}(2\beta\delta^{-1} + 1)^{p-1}}.$$

Step  $k$ : Assume we have determined an  $m_{k-1} \in \mathbb{N}$  such that, if  $m \geq m_{k-1}$ , we can guarantee

$$d(\mathbb{G}^{k-1}, \hat{\mathbb{G}}^{k-1}) \leq \frac{\epsilon}{2^{p-k+1}(2\beta\delta^{-1} + 1)^{p-k+1}}$$

with probability at least  $1 - 2^{-(j+2(p-k+1))}$ . By the definition of  $\mathbb{U}^k$  and  $\hat{\mathbb{U}}^k$ , these two spaces can be identified with subspaces  $\mathbb{H}^k, \hat{\mathbb{H}}^k \subset \mathbb{R}^{n_1 \dots n_k}$ , and Lemma 3 shows that  $d(\mathbb{H}^k, \hat{\mathbb{H}}^k)$  satisfies the same bound with the same probability. Now, we choose an orthonormal basis  $V_k \in \mathbb{R}^{n_1 \dots n_k \times r_{k-1} n_k}$  of  $\mathbb{H}^k$ , and obtain a basis  $\hat{V}_k$  for  $\hat{\mathbb{H}}^k$  by the orthogonal projection (in Euclidean space) of the columns of  $V_k$  onto  $\hat{\mathbb{H}}^k$ . Using the corresponding bases in function space to calculate the Galerkin matrices, Lemma 4 now yields the estimate:

$$\|\hat{C}_{\hat{\mathbb{U}}^k}^{00} - C_{\mathbb{U}^k}^{00}\|_2 \leq 2\|\hat{C}_{\mathbb{S}^k}^{00}\|_2 d(\mathbb{H}^k, \hat{\mathbb{H}}^k) + \|\hat{C}_{\mathbb{U}^k}^{00} - C_{\mathbb{U}^k}^{00}\|_2. \quad (14)$$

We can apply the Davis-Kahan-Theorem to the dominant eigenspaces  $\mathbb{J}^k, \hat{\mathbb{J}}^k$  of the matrices  $\hat{C}_{\mathbb{U}^k}^{00}$  and  $C_{\mathbb{U}^k}^{00}$  in  $\mathbb{R}^{r_{k-1}n_k}$ . Combining this with Lemma 5, we end up with the estimate

$$d(\mathbb{G}^k, \hat{\mathbb{G}}^k) \leq d(\mathbb{J}^k, \hat{\mathbb{J}}^k) + d(\mathbb{H}^k, \hat{\mathbb{H}}^k) \quad (15)$$

$$\leq \left[ \frac{2}{\delta} \|\hat{C}_{\mathbb{S}^k}^{00}\|_2 + 1 \right] d(\mathbb{H}^k, \hat{\mathbb{H}}^k) + \frac{1}{\delta} \|\hat{C}_{\mathbb{U}^k}^{00} - C_{\mathbb{U}^k}^{00}\|_2. \quad (16)$$

Using the induction hypothesis, ergodicity of the process, and Lemma 6, we can choose an  $m_k \geq m_{k-1}$  such that, for  $m \geq m_k$  and with probability at least  $1 - 2^{-(j+2(p-k))}$ , we simultaneously have

$$\|\hat{C}_{\mathbb{S}^k}^{00}\|_2 \leq \beta, \quad d(\mathbb{H}^k, \hat{\mathbb{H}}^k) \leq \frac{\epsilon}{2^{p-k+1}(2\beta\delta^{-1} + 1)^{p-k+1}}, \quad \|\hat{C}_{\mathbb{U}^k}^{00} - C_{\mathbb{U}^k}^{00}\|_2 \leq \frac{\epsilon\delta}{2^{p-k+1}(2\beta\delta^{-1} + 1)^{p-k}}.$$

Then, it follows from (15) that

$$\mathbb{P} \left[ d(\mathbb{G}^k, \hat{\mathbb{G}}^k) \leq \frac{\epsilon}{2^{p-k}(2\beta\delta^{-1} + 1)^{p-k}} \right] \geq 1 - 2^{-(j+2(p-k))}. \quad (17)$$

Applying (17) with  $k = p$  yields  $d(\mathbb{G}^p, \hat{\mathbb{G}}^p) \leq \epsilon$  with probability greater than  $1 - 2^{-j}$ , which concludes the proof.  $\square$

**Corollary 1:** *For infinite data, application of AMUSEt to decompositions (9) of  $\Psi(X)$  (and  $\Psi(Y)$ ) converges to a Galerkin approximation of the Koopman operator for EDMD (Forward-backward operator for CCA) onto fixed subspaces.*

## 4 Numerical examples

We apply the data-driven tensor-decomposition methods developed in the previous section to two benchmarking data sets of molecular dynamics simulation. Both of these systems have been analyzed before, using standard methods in the field, providing reference values which serve as comparison for our results. We demonstrate that our algorithms enable us to work on large trial spaces where the full calculation of the empirical Galerkin matrices is very hard or impossible. Furthermore, we also test the tensor CCA algorithm by applying it to the ABC flow, which has served as a model system for fluid dynamics problems in various previous studies.

The numerical experiments have been performed on a Linux machine with 128 GB RAM and an Intel Xeon processor with a clock speed of 3 GHz and 8 cores. The algorithms have been implemented in Python 3.6 and collected in the toolbox Scikit-TT<sup>1</sup>. Furthermore, we used d3s<sup>2</sup>, PyEMMA<sup>3</sup> [44] as well as scikit-image<sup>4</sup> for simulating and analyzing the numerical examples.

### 4.1 Deca-alanine

We re-analyze molecular dynamics simulation data of deca-alanine peptide in explicit water (see [32] for the simulation setup). The downsampled data set we use comprises  $m = 6000$  frames at a time spacing of 500 ps. As the system is reversible and stationary, we can apply EDMD with a single approximation space  $\mathbb{V}$ . We choose  $p = 10$  elementary subspaces  $\mathbb{V}^k$ , each of them spanned by either  $n_k = 3$  or  $n_k = 4$  functions of a single dihedral angle of the peptide. These functions always include the constant and two or three periodic Gaussians of the form

$$\psi_{k,i_k}(x_k) = \exp \left[ -\frac{1}{2s_{i_k}} \sin^2(0.5(x_k - c_{i_k})) \right].$$

<sup>1</sup>[https://github.com/PGelss/scikit\\_tt](https://github.com/PGelss/scikit_tt)

<sup>2</sup><https://github.com/sklus/d3s>

<sup>3</sup><http://www.emma-project.org>

<sup>4</sup><http://www.scikit-image.org/>

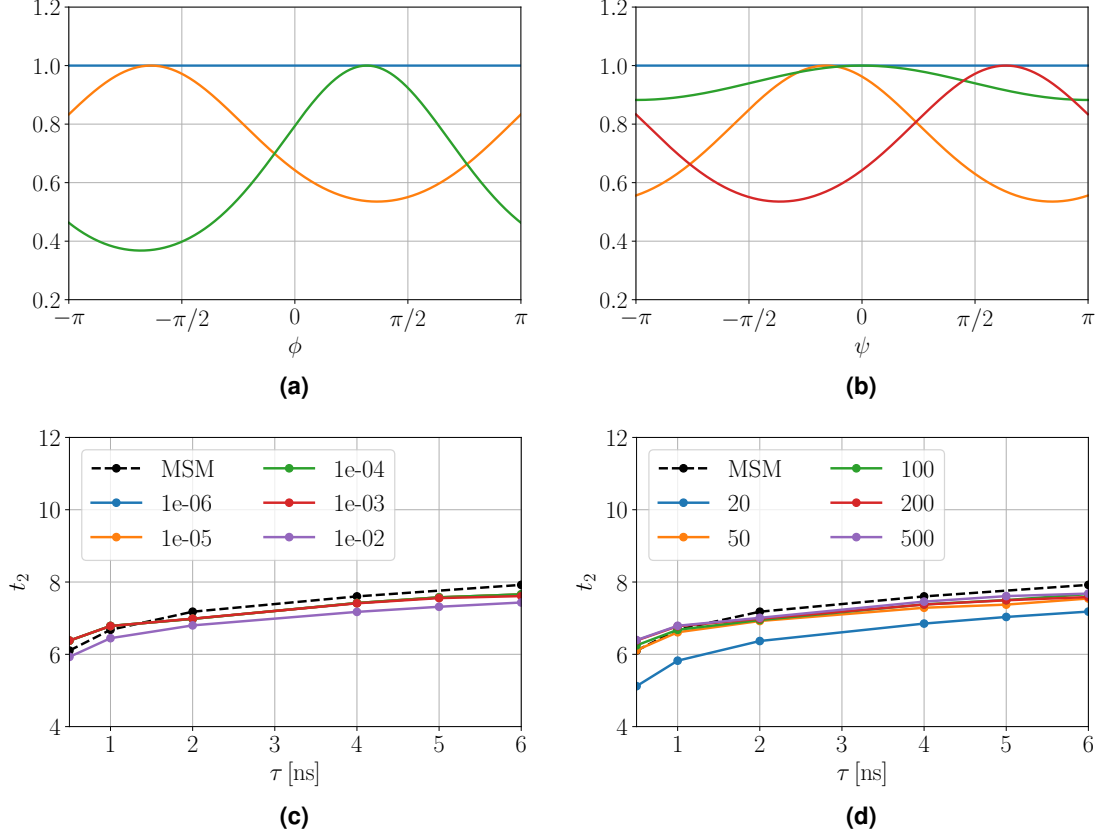


**Figure 6:** Results for molecular dynamics simulation data of deca-alanine peptide: (a) Univariate basis set used for all  $\phi$ -dihedral angles, comprised of the constant and periodic Gaussians centered at  $c_{i_k} = \{-2, 1\}$ , with  $s_{i_k} = \{0.8, 0.5\}$ . (b) The same for all  $\psi$ -dihedral angles, where periodic Gaussians are centered at  $c_{i_k} = \{-0.5, 0.0, 2.0\}$ , with  $s_{i_k} = \{0.8, 4.0, 0.8\}$ . (c) Slowest timescale  $t_2$  obtained from (13) after constructing  $\Psi(Z)$  using the exact TT decomposition given in (9). We show results for different values of relative SVD truncation parameter  $\varepsilon$  and as a function of the lag time  $\tau$ . The reference MSM is represented by the black line. (d) The same if  $\Psi(Z)$  is represented by the HOCUR algorithm, for different values of the maximal rank in Algorithm 3.

Their positions and shapes are chosen to align with the typical marginal distribution of protein data along its backbone dihedral angles, see Figures 6 (a) and (b). The full tensor space  $\mathbb{V}$  is then of dimension  $N = 3^5 \cdot 4^5 \approx 2.5 \cdot 10^5$ .

We use the direct decomposition (9) and the HOCUR decomposition (Section 3.1) to arrive at TT representations of the transformed data tensor  $\Psi(Z)$ . Subsequently, the procedure outlined in Section 3.2 is applied to obtain eigenvalues and eigenfunctions of the reduced problem (13). We repeat this procedure for a series of lag times  $\tau$ , and convert the eigenvalues  $\lambda_k(\tau)$  of (13) into estimates for implied timescales by the formula

$$t_k = -\frac{\tau}{\log(\lambda_k(\tau))}.$$

We monitor the slowest implied timescale  $t_2$  as a function of  $\tau$ . The results are compared to a Markov state model (MSM) using 500 discrete states. The latter was built by following a typical protocol from the literature (linear dimension reduction by TICA, followed by k-means clustering in reduced space), see [45].

When working with the HOSVD method, a crucial parameter is the relative truncation threshold  $\varepsilon$  used during the global SVD calculation which serves as a regularization parameter. In Figure 6 (c), we compare estimates of  $t_2$  obtained for different values of  $\varepsilon$ . We note that all results agree well with the reference as  $\varepsilon$  varies between  $10^{-6}$  and  $10^{-3}$ . However, the maximal rank of these TT representations differs by about an order of magnitude: for  $\varepsilon = 10^{-5}$ , we have  $r_p = 1018$ , while for



$\varepsilon = 10^{-3}$ ,  $r_p = 109$ . Moreover, timescale estimates increase as  $\varepsilon$  decreases, which follows from the variational principle (6) and Proposition 1, as a smaller threshold leads to a larger subspace selected during the global SVD.

For HOCUR, a natural hyper-parameter to monitor is the maximal rank allowed in Algorithm 3, while the relative truncation threshold is fixed to  $\varepsilon = 10^{-4}$ . We find that using a rank as low as 50 provides excellent agreement of the slowest timescale with the reference, see Figure 6 (d). In this example, both methods provide efficient tensor train representations which capture the slow dynamics of the peptide.

## 4.2 NTL9

The second example we study is a set of four equilibrium molecular dynamics simulations of 39 residue protein NTL9 in explicit water. The data were produced by D. E. Shaw Research on the Anton Supercomputer [46]. The downsampled data set comprises approximately 1.4 million frames at a time spacing of 2 ns. The MSM analysis presented in [47] serves as reference model.

We consider the feature set of closest heavy-atom distances between residues. Furthermore, we define a contact between two residues to have formed if their distance is smaller than 0.35 nm. After ranking all features by the fraction of simulation time during which the contact was formed, we choose the first  $p = 20$  distance features as domains for the univariate trial functions. Elementary function spaces  $\mathbb{V}^k$  are then defined by the constant and two Gaussian functions of the form

$$\psi_{k,i_k}(x_k) = \exp\left[-\frac{1}{2s_{i_k}}(x_k - c_{i_k})^2\right],$$

centered along each distance coordinate  $x_k$ , see Figure 7 (a). The parameters of the Gaussians were chosen so that the distribution of all distances in the data set can be reproduced by a linear combination of these basis functions. We thus have  $n_k = 3$  for  $k = 1, \dots, p$ , the full tensor space is of dimension  $N = 3^{20} \approx 3.5 \cdot 10^9$ . We also compute tensor-based models using only the first  $p = 10$  distances, corresponding to a tensor space of dimension  $N = 3^{10} = 59049$ .

Just as before, we use both the direct decomposition (9) and the HOCUR iteration to represent the data tensor  $\Psi(Z)$ . For a series of lag times  $\tau$ , global SVD at relative truncation parameter  $\varepsilon = 10^{-3}$  is then applied to  $\Psi(X)$  and the reduced matrix  $M$  (13) is computed. After diagonalizing  $M$ , we extract estimates of the slowest timescale  $t_2$  and evaluate the first two eigenfunctions on the data as shown in Figure 5.

In Figure 7 (b), we monitor the estimated slowest timescale  $t_2$  as a function of the lag time. We find that it indeed converges towards the reference value with increasing lag time for all tensor based models we are considering. When using the direct decomposition (9), we can run the algorithm within a few minutes if we reduce the data size to  $m = 56,000$  frames. However, we cannot increase the number of distances or the data size much beyond these limits without a significant increase of computational time and memory requirement. The major computational bottleneck here is the repeated application of SVDs to large matrices. Interestingly, we can push these limitations further when working with the HOCUR iteration, as it only requires the evaluation of a limited number of tensor entries during the course of the algorithm. We find that the iteration completes within about an hour for  $p = 20$  dimensions and all  $m \approx 1.4 \cdot 10^6$  data points. Moreover, the maximum rank for the HOCUR approach is much smaller than the TT ranks of the (left-orthonormalized) transformed data tensors produced by the HOSVD approach. That is, the maximum ranks for the application of Algorithm 3 are set to 1000 while the resulting maximum rank of the direct decomposition (9) after left-orthonormalization is larger than 3600.

The point of this example is not to outperform the analysis in [47], but rather to test the capabilities and limitations of both tensor decompositions presented in this work as the tensor dimension  $p$  and the number of snapshots  $m$  are increased. The MSM provides a more refined model than our approximations, but its construction requires a higher level of expertise and user intervention. A more natural comparison is the direct application of linear TICA [48] to a varying number of distance coordinates. We note that it takes at least 200 distances to achieve the same approximation quality as any of the tensor-based models we considered here. When using only 20 distances for TICA, the computed timescales barely approach the reference value obtained by applying MSM.

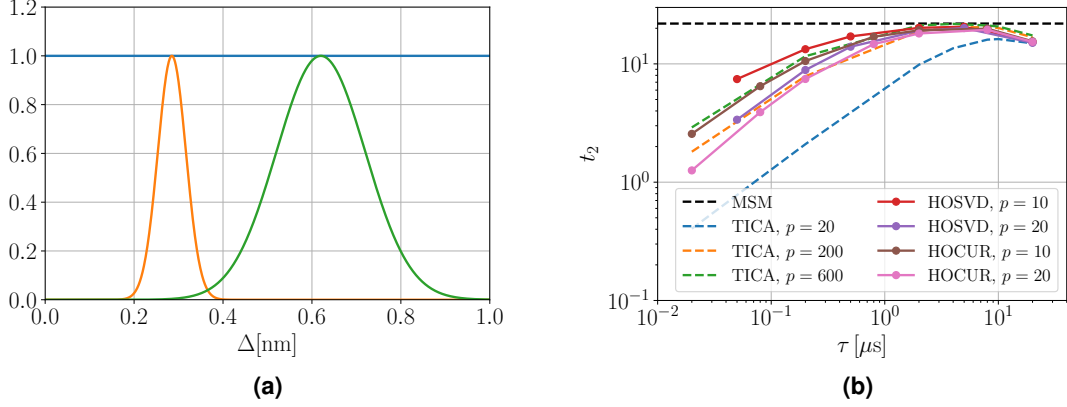


**Figure 7:** Results for molecular dynamics simulation data of NTL9 protein: (a) Univariate basis set used for all distance coordinates, comprised of the constant and Gaussian functions centered at  $c_{i_k} = \{0.285, 0.62\}$ , with  $s_{i_k} = \{0.001, 0.01\}$ . (b) Slowest timescale obtained from (13) after representing the data tensor  $\Psi(Z)$  either using the exact decomposition or by Algorithm 3. For the direct method, we consider approximately 56000 data points, while more than  $1.4 \cdot 10^6$  data points were used for HOCUR. The MSM-based reference value as well as the timescales computed by TICA are indicated by the dashed lines.

The fact that we can use tensor decompositions to analyze a large data set of a complex system using a huge number of basis functions ( $N = 3^{20}$ ) on limited computational resources is an encouraging result.

For completeness, we also verify that the second eigenfunction estimated by AMUSEt correctly encodes the folding process of NTL9. To this end, we apply PCCA [49] to the time series of the first two eigenfunctions and assign each snapshot to one of two metastable states if the degree of membership exceeds 0.5. We then calculate the contact probabilities separately for each of the two states. These so-called contact maps are shown in the upper left triangles of Figures 8 (a) and (b). By comparing to the contact maps provided by the reference model (lower right triangles in Figures 8 (a) and (b)), we see that there is virtually no difference. In Figures 8 (c) and (d), we also show representative structures for the unfolded and folded state, respectively. The results shown in Figures 8 are based on the HOCUR model at  $p = 20$ , but we have verified that the same results can be obtained if the direct model is analyzed.

### 4.3 ABC flow

In order to illustrate the computation of coherent sets using tensor CCA, let us consider the well-known ABC (Arnold–Beltrami–Childress) flow, given by the ordinary differential equation

$$\begin{aligned} \dot{z}_1 &= A \sin(z_3) + C \cos(z_2), \\ \dot{z}_2 &= B \sin(z_1) + A \cos(z_3), \\ \dot{z}_3 &= C \sin(z_2) + B \cos(z_1), \end{aligned}$$

with  $A = \sqrt{3}$ ,  $B = \sqrt{2}$ , and  $C = 1$ . The system is defined on the torus, i.e.,  $0 \leq z_i \leq 2\pi$  for  $i = 1, 2, 3$ , see [50] for details. We define the lag time to be  $\tau = 5$  and sample  $25^3$  test points  $x_i$  uniformly in  $[0, 2\pi]^3$ . In order to compute the corresponding points  $y_i$ , we use a standard Runge–Kutta integrator with variable step size. Thus,  $X, Y \in \mathbb{R}^{3 \times 15625}$ . Using a coordinate-major decomposition comprising ten Gaussian functions with variance 1 in each dimension (resulting in 1000 three-dimensional Gaussians on an equidistant grid), we apply AMUSEt for tensor-based CCA as described in Section 3.3. Here, we use scikit-image in order to extract isosurfaces from the computed eigenfunctions. The coherent sets shown in Figure 9 are consistent with the results presented in [36].

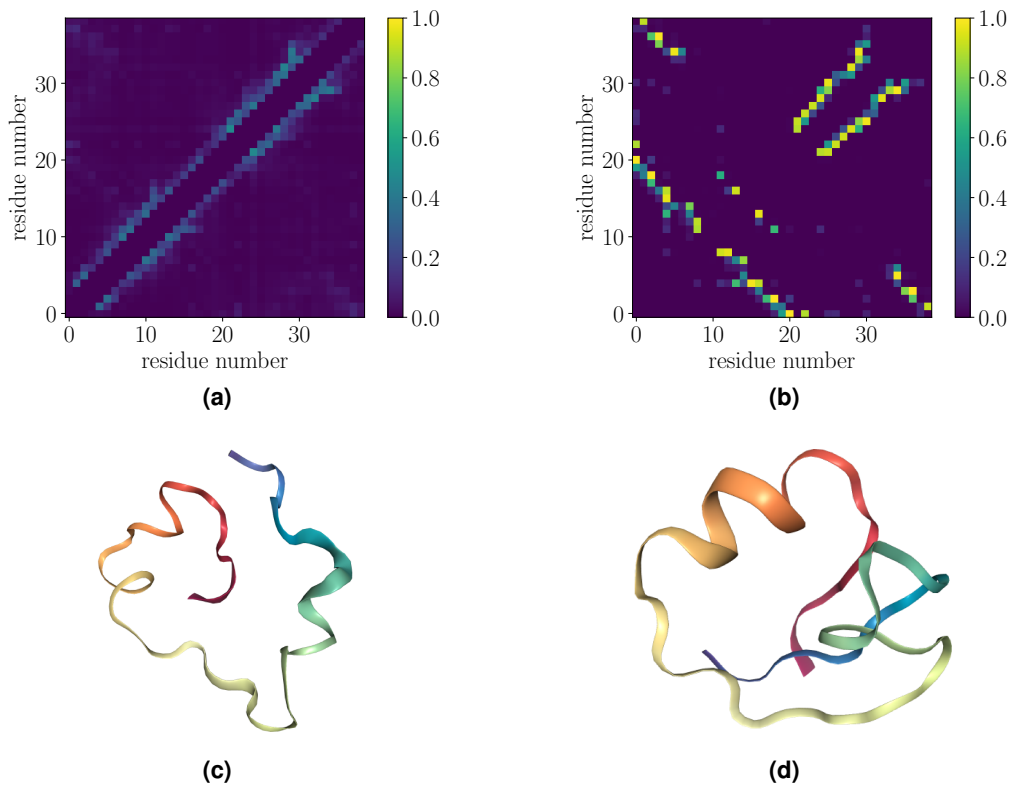


**Figure 8:** States of NTL9: (a) Contact map for the unfolded state computed from the first two eigenfunctions of the HOCUR model at lag time  $\tau = 5 \mu\text{s}$  (upper left triangle), compared to the corresponding contact map of the reference MSM (lower right triangle). (b) The same for the folded state. (c)/(d) Representative molecular structures for the unfolded and folded state of NTL9.

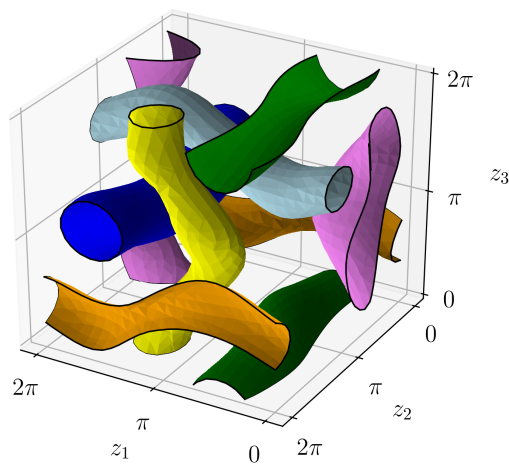


**Figure 9:** Results for ABC flow: Six coherent vortices in the domain, extracted by applying tCCA.

## 5 Summary

We have presented different techniques to approximate the Koopman operator associated with high-dimensional dynamical systems using tensor-structured basis sets. Two tensor train representations of the transformed data tensor for such a basis set were introduced. We have provided a detailed algorithmic description of an iterative method to compute a higher-order CUR decomposition, which only requires evaluations of the basis set on the data. Moreover, we have derived an efficient method to solve the eigenvalue problem for the Koopman operator based on TT representations of the data. The size of the resulting matrix eigenvalue problem does not exceed the number of snapshots in the data. We have presented an extension of this algorithm to the calculation of coherent sets using tensor-based CCA. By proving convergence of the method in the infinite data limit, a physical interpretation of the method was provided. We have also presented successful applications to benchmarking data sets of molecular dynamics simulation and fluid dynamics. In one of these examples, we found that HOCUR decompositions were still able to provide accurate solutions in a setting where the direct HOSVD based method would become intractable. To the best of our knowledge, we have presented the first application of HOCUR in the field of the data-driven analysis of dynamical systems.

## Acknowledgements

This research has been funded by the National Science Foundation (CHE-1265929, CHE-1738990, CHE-1900374, PHY-1427654) [FN, CC], the Welch Foundation (C-1570) [FN, CC], the Rice University Academy of Fellows [FN], Deutsche Forschungsgemeinschaft (CRC 1114, “Scaling Cascades in Complex Systems”) [PG, SK], and the Einstein Foundation Berlin [CC]. The authors are grateful to D. E. Shaw Research for providing the NTL9 simulation data.

## A Details of the Proof of Proposition 1

In this appendix, we provide the technical lemmas used in the proof of Prop. 1. The first result is used to calculate the distance between the spaces  $\mathbb{H}^k, \hat{\mathbb{H}}^k$ .

**Lemma 3:** *Given  $r$ -dimensional vector spaces  $\mathbb{G}, \hat{\mathbb{G}} \subset \mathbb{R}^{N_1}$  such that  $d(\mathbb{G}, \hat{\mathbb{G}}) \leq \epsilon$ . Define  $\mathbb{H} = \mathbb{G} \otimes \mathbb{R}^{N_2}$  and  $\hat{\mathbb{H}} = \hat{\mathbb{G}} \otimes \mathbb{R}^{N_2}$ . Then  $d(\mathbb{H}, \hat{\mathbb{H}}) \leq \epsilon$  in  $\mathbb{R}^{N_1 N_2}$ .*

*Proof.* Choose orthonormal bases  $U, \hat{U} \in \mathbb{R}^{N_1 \times r}$  for  $\mathbb{G}$  and  $\hat{\mathbb{G}}$ , respectively. Then,  $U \otimes \text{Id}_{N_2}$  and  $\hat{U} \otimes \text{Id}_{N_2}$  are orthonormal bases for  $\mathbb{H}, \hat{\mathbb{H}}$ . We calculate the distance using orthogonal projectors:

$$\begin{aligned} d(\mathbb{H}, \hat{\mathbb{H}}) &= \|\text{Id}_{N_1 N_2} - (\hat{U} \otimes \text{Id}_{N_2})(\hat{U} \otimes \text{Id}_{N_2})^T U \otimes \text{Id}_{N_2}\|_2 \\ &= \|\text{Id}_{N_1} \otimes \text{Id}_{N_2} - (\hat{U} \hat{U}^T \otimes \text{Id}_{N_2}) U \otimes \text{Id}_{N_2}\|_2 \\ &= \|U \otimes \text{Id}_{N_2} - (\hat{U} \hat{U}^T U \otimes \text{Id}_{N_2})\|_2 \\ &= \|[(\text{Id}_{N_1} - \hat{U} \hat{U}^T) U] \otimes \text{Id}_{N_2}\|_2 \\ &= \|[(\text{Id}_{N_1} - \hat{U} \hat{U}^T) U]\|_2 = d(\mathbb{G}, \hat{\mathbb{G}}). \quad \square \end{aligned}$$

We prove estimate (14):

**Lemma 4:** *Choose an orthonormal basis  $V_k$  for  $\mathbb{H}_k$ , and define  $\hat{V}_k$  as the orthogonal projection of  $V_k$  onto  $\hat{\mathbb{H}}^k$ , as described in the proof of Proposition 1. Then we obtain the estimate:*

$$\|\hat{C}_{\hat{U}^k}^{00} - C_{U^k}^{00}\|_2 \leq 2\|\hat{C}_{S^k}^{00}\|_2 d(\mathbb{H}^k, \hat{\mathbb{H}}^k) + \|\hat{C}_{U^k}^{00} - C_{U^k}^{00}\|_2. \quad (18)$$

*Proof.*

$$\begin{aligned} \|\hat{C}_{\hat{U}^k}^{00} - C_{U^k}^{00}\|_2 &\leq \|\hat{C}_{\hat{U}^k}^{00} - \hat{C}_{U^k}^{00}\|_2 + \|\hat{C}_{U^k}^{00} - C_{U^k}^{00}\|_2 \\ &= \|\hat{V}_k^T \hat{C}_{S^k}^{00} \hat{V}_k - V_k^T \hat{C}_{S^k}^{00} V_k\|_2 + \|\hat{C}_{U^k}^{00} - C_{U^k}^{00}\|_2 \end{aligned}$$

$$\begin{aligned}
&\leq \|(\hat{V}_k^T - V_k^T)\hat{C}_{\mathbb{S}^k}^{00}\hat{V}_k\|_2 + \|V_k^T\hat{C}_{\mathbb{S}^k}^{00}(\hat{V}_k - V_k)\|_2 + \|\hat{C}_{\mathbb{U}^k}^{00} - C_{\mathbb{U}^k}^{00}\|_2 \\
&\leq 2\|\hat{C}_{\mathbb{S}^k}^{00}\|_2\|V_k - \hat{V}_k\|_2 + \|\hat{C}_{\mathbb{U}^k}^{00} - C_{\mathbb{U}^k}^{00}\|_2,
\end{aligned}$$

where we used that  $\|V_k\|_2 = 1$  and  $\|\hat{V}_k\|_2 \leq 1$  by construction. Moreover, since we constructed  $\hat{V}_k$  by the best-approximation of  $V_k$  in  $\hat{\mathbb{H}}^k$ , we have:

$$\begin{aligned}
\|V_k - \hat{V}_k\|_2 &= \sup_{\|x\|=1} \|V_k x - \hat{V}_k x\| = \sup_{\|x\|=1} \inf_y \|V_k x - \hat{V}_k y\| \\
&= \sup_{\|V_k x\|=1} \inf_y \|V_k x - \hat{V}_k y\| = d(\mathbb{H}^k, \hat{\mathbb{H}}^k),
\end{aligned}$$

completing the proof.  $\square$

**Lemma 5:** Consider the dominant eigenspaces  $\mathbb{J}^k, \hat{\mathbb{J}}^k$  of the matrices  $\hat{C}_{\mathbb{U}^k}^{00}$  and  $C_{\mathbb{U}^k}^{00}$ . The distance between these spaces translates into an estimate for  $d(\mathbb{G}^k, \hat{\mathbb{G}}^k)$  as follows:

$$d(\mathbb{G}^k, \hat{\mathbb{G}}^k) \leq d(\mathbb{J}^k, \hat{\mathbb{J}}^k) + d(\mathbb{H}^k, \hat{\mathbb{H}}^k).$$

*Proof.* By definition, bases of the spaces  $\mathbb{G}^k$  and  $\hat{\mathbb{G}}^k$  are obtained by taking basis sets  $W_k, \hat{W}_k$  of  $\mathbb{J}^k, \hat{\mathbb{J}}^k$ , and then taking the products  $V_k W_k$  and  $\hat{V}_k \hat{W}_k$ . We introduce the intermediate space  $\tilde{\mathbb{G}}^k$  with basis  $V_k \hat{W}_k$ . Using that the matrix  $V_k$  is orthonormal, and the best-approximation property of  $\hat{V}_k$ , we find:

$$\begin{aligned}
d(\mathbb{G}^k, \tilde{\mathbb{G}}^k) &= \sup_{x, \|V_k W_k x\|=1} \inf_y \|V_k W_k x - V_k \hat{W}_k y\| \\
&= \sup_{x, \|W_k x\|=1} \inf_y \|W_k x - \hat{W}_k y\| = d(\mathbb{J}^k, \hat{\mathbb{J}}^k), \\
d(\tilde{\mathbb{G}}^k, \hat{\mathbb{G}}^k) &= \sup_{x, \|V_k \hat{W}_k x\|=1} \inf_y \|V_k \hat{W}_k x - \hat{V}_k \hat{W}_k y\| \\
&= \sup_{x, \|V_k \hat{W}_k x\|=1} \|V_k \hat{W}_k x - \hat{V}_k \hat{W}_k x\| \leq d(\mathbb{H}^k, \hat{\mathbb{H}}^k).
\end{aligned}$$

The claim follows from the triangle inequality for the distance between subspaces.  $\square$

The last result is elementary:

**Lemma 6:** Let  $A_1, A_2, A_3$  be events in a probability space with  $\mathbb{P}(A_i) \geq 1 - 2^{-(j+2)}$  for  $i = 1, 2, 3$ . Then

$$\mathbb{P}(A_1 \cap A_2 \cap A_3) \geq 1 - 2^{-j}.$$

*Proof.* This follows by twice applying the elementary inequality

$$\begin{aligned}
1 &\geq \mathbb{P}(A_1 \cup A_2) = \mathbb{P}(A_1) + \mathbb{P}(A_2) - \mathbb{P}(A_1 \cap A_2) \geq 2(1 - 2^{-(j+2)}) - \mathbb{P}(A_1 \cap A_2) \\
&\Leftrightarrow \mathbb{P}(A_1 \cap A_2) \geq 1 - 2^{-(j+1)}.
\end{aligned}$$

$\square$

## References

- [1] C. Schütte, A. Fischer, W. Huisinga, and P. Deuffhard. A direct approach to conformational dynamics based on hybrid Monte Carlo. *Journal of Computational Physics*, 151(1):146–168, 1999. doi:10.1006/jcph.1999.6231.
- [2] M. Dellnitz and O. Junge. On the approximation of complicated dynamical behavior. *SIAM Journal on Numerical Analysis*, 36(2):491–515, 1999. doi:10.1137/S0036142996313002.
- [3] C. W. Rowley, I. Mezić, S. Bagheri, P. Schlatter, and D. S. Henningson. Spectral analysis of nonlinear flows. *Journal of Fluid Mechanics*, 641:115–127, 2009. doi:10.1017/S0022112009992059.
- [4] M. Budišić, R. Mohr, and I. Mezić. Applied Koopmanism. *Chaos: An Interdisciplinary Journal of Non-linear Science*, 22(4):047510, 2012. doi:10.1063/1.4772195.

- [5] S. Klus, F. Nüske, P. Koltai, H. Wu, I. Kevrekidis, C. Schütte, and F. Noé. Data-driven model reduction and transfer operator approximation. *Journal of Nonlinear Science*, 28(3):985–1010, 2018. doi:10.1007/s00332-017-9437-7.
- [6] M. O. Williams, I. G. Kevrekidis, and C. W. Rowley. A data-driven approximation of the Koopman operator: Extending dynamic mode decomposition. *Journal of Nonlinear Science*, 25(6):1307–1346, 2015. doi:10.1007/s00332-015-9258-5.
- [7] S. Klus, P. Koltai, and C. Schütte. On the numerical approximation of the Perron–Frobenius and Koopman operator. *Journal of Computational Dynamics*, 3(1):51–79, 2016. doi:10.3934/jcd.2016003.
- [8] F. Noé and F. Nüske. A variational approach to modeling slow processes in stochastic dynamical systems. *Multiscale Modeling & Simulation*, 11:635–655, 2013. doi:10.1137/110858616.
- [9] F. Nüske, B. G. Keller, G. Pérez-Hernández, A. S. J. S. Mey, and F. Noé. Variational approach to molecular kinetics. *Journal of Chemical Theory and Computation*, 10:1739–1752, 2014. doi:10.1021/ct4009156.
- [10] G. Froyland, N. Santitissadeekorn, and A. Monahan. Transport in time-dependent dynamical systems: Finite-time coherent sets. *Chaos: An Interdisciplinary Journal of Nonlinear Science*, 20(4):043116, 2010.
- [11] G. Froyland. An analytic framework for identifying finite-time coherent sets in time-dependent dynamical systems. *Physica D: Nonlinear Phenomena*, 250:1–19, 2013.
- [12] D. R. Hardoon, S. Szedmak, and J. Shawe-Taylor. Canonical correlation analysis: An overview with application to learning methods. *Neural computation*, 16(12):2639–2664, 2004.
- [13] S. Klus, B. E. Husic, M. Mollenhauer, and F. Noé. Kernel methods for detecting coherent structures in dynamical data. *Chaos*, 2019. doi:10.1063/1.5100267.
- [14] M. O. Williams, C. W. Rowley, and I. G. Kevrekidis. A kernel-based method for data-driven Koopman spectral analysis. *Journal of Computational Dynamics*, 2(2):247–265, 2015. doi:10.3934/jcd.2015005.
- [15] S. Klus, I. Schuster, and K. Muandet. Eigendecompositions of transfer operators in reproducing kernel Hilbert spaces. *ArXiv e-prints*, 2017. arXiv:1712.01572v2.
- [16] A. Mardt, L. Pasquali, H. Wu, and F. Noé. VAMPnets for deep learning of molecular kinetics. *Nature communications*, 9(1):5, 2018. doi:10.1038/s41467-017-02388-1.
- [17] J. D. Carroll and J. J. Chang. Analysis of individual differences in multidimensional scaling via an N-way generalization of ‘Eckart-Young’ decomposition. *Psychometrika*, 35(3):283–319, 1970. doi:10.1007/BF02310791.
- [18] L. R. Tucker. The extension of factor analysis to three-dimensional matrices. In H. Gulliksen and N. Frederiksen, editors, *Contributions to mathematical psychology*, pages 110–127. Holt, Rinehart and Winston, 1964.
- [19] W. Hackbusch and S. Kühn. A new scheme for the tensor representation. *Journal of Fourier analysis and applications*, 15(5):706–722, 2009. doi:10.1007/s00041-009-9094-9.
- [20] I. Oseledets and E. Tyrtshnikov. Breaking the curse of dimensionality, or how to use SVD in many dimensions. *SIAM Journal on Scientific Computing*, 31(5):3744–3759, 2009. doi:10.1137/090748330.
- [21] I. Oseledets. Tensor-train decomposition. *SIAM Journal on Scientific Computing*, 33:2295–2317, 2011. doi:10.1137/090752286.
- [22] M. H. Beck, A. Jäckle, G. A. Worth, and H. D. Meyer. The multiconfiguration time-dependent Hartree (MCTDH) method: a highly efficient algorithm for propagating wavepackets. *Physics Reports*, 324:1–105, 2000. doi:10.1016/S0370-1573(99)00047-2.
- [23] S. Dolgov and B. Khoromskij. Simultaneous state-time approximation of the chemical master equation using tensor product formats. *Numerical Linear Algebra with Applications*, 22(2):197–219, 2015. doi:10.1002/nla.1942.
- [24] P. Gelß, S. Matera, and C. Schütte. Solving the master equation without kinetic Monte Carlo. *Journal of Computational Physics*, 314(C):489–502, 2016. doi:10.1016/j.jcp.2016.03.025.
- [25] Z. Zhang, K. Batselier, H. Liu, L. Daniel, and N. Wong. Tensor computation: A new framework for high-dimensional problems in EDA. *IEEE Transactions on Computer-Aided Design of Integrated Circuits and Systems*, 36(4):521–536, 2017. doi:10.1109/TCAD.2016.2618879.
- [26] P. Gelß, S. Klus, J. Eisert, and C. Schütte. Multidimensional approximation of nonlinear dynamical systems. *Journal of Computational and Nonlinear Dynamics*, 14(6):061006, 2019. doi:10.1115/1.4043148.



- [27] I. Affleck, T. Kennedy, E. H. Lieb, and H. Tasaki. Rigorous results on valence-bond ground states in antiferromagnets. *Physical Review Letters*, 59(7):799–802, 1987. doi:10.1103/PhysRevLett.59.799.
- [28] S. Östlund and S. Rommer. Thermodynamic limit of density matrix renormalization. *Physical Review Letters*, 75(19):3537, 1995. doi:10.1103/PhysRevLett.75.3537.
- [29] S. Szalay, M. Pfeffer, V. Murg, G. Barcza, F. Verstraete, R. Schneider, and Ö Legeza. Tensor product methods and entanglement optimization for ab initio quantum chemistry. *International Journal of Quantum Chemistry*, 115(19):1342–1391, 2015. doi:10.1002/qua.24898.
- [30] F. Litzinger, L. Boninsegna, H. Wu, F. Nüske, R. Patel, R. Baraniuk, F. Noé, and C. Clementi. Rapid calculation of molecular kinetics using compressed sensing. *Journal of Chemical Theory and Computation*, 14(5):2771–2783, 2018. doi:10.1021/acs.jctc.8b00089.
- [31] S. Klus and C. Schütte. Towards tensor-based methods for the numerical approximation of the Perron–Frobenius and Koopman operator. *Journal of Computational Dynamics*, 3(2):139–161, 2016. doi:10.3934/jcd.2016007.
- [32] F. Nüske, R. Schneider, F. Vitalini, and F. Noé. Variational tensor approach for approximating the rare-event kinetics of macromolecular systems. *Journal of Chemical Physics*, 144(5):054105, 2016. doi:10.1063/1.4940774.
- [33] L. Tong, V. C. Soon, Y. F. Huang, and R. Liu. AMUSE: a new blind identification algorithm. In *IEEE international symposium on circuits and systems*, pages 1784–1787. IEEE, 1990. doi:10.1109/ISCAS.1990.111981.
- [34] S. Klus, P. Gelß, S. Peitz, and C. Schütte. Tensor-based dynamic mode decomposition. *Nonlinearity*, 31(7), 2018. doi:10.1088/1361-6544/aabc8f.
- [35] I. Oseledets and E. Tyrtyshnikov. TT-cross approximation for multidimensional arrays. *Linear Algebra and its Applications*, 432(1):70–88, 2010. doi:10.1016/j.laa.2009.07.024.
- [36] R. Banisch and P. Koltai. Understanding the geometry of transport: Diffusion maps for Lagrangian trajectory data unravel coherent sets. *Chaos: An Interdisciplinary Journal of Nonlinear Science*, 27(3):035804, 2017. doi:10.1063/1.4971788.
- [37] R. Penrose. Applications of negative dimensional tensors. *Combinatorial mathematics and its applications*, 1:221–244, 1971.
- [38] P. Gelß, S. Klus, S. Matera, and C. Schütte. Nearest-neighbor interaction systems in the tensor-train format. *Journal of Computational Physics*, 341:140–162, 2017. doi:10.1016/j.jcp.2017.04.007.
- [39] C. Boutsidis and D. P. Woodruff. Optimal CUR matrix decompositions. In *Proceedings of the Forty-sixth Annual ACM Symposium on Theory of Computing*, STOC '14, pages 353–362. ACM, 2014. doi:10.1145/2591796.2591819.
- [40] S. A. Goreinov, I. V. Oseledets, D. V. Savostyanov, E. E. Tyrtyshnikov, and N. L. Zamarashkin. How to find a good submatrix. In *Matrix Methods: Theory, Algorithms And Applications: Dedicated to the Memory of Gene Golub*, pages 247–256. World Scientific, 2010. doi:10.1142/9789812836021\_0015.
- [41] S. A. Goreinov and E. E. Tyrtyshnikov. The maximal-volume concept in approximation by low-rank matrices. In V. Olshevsky, editor, *Structured Matrices in Mathematics, Computer Science, and Engineering I*, volume 280, pages 47–51. American Mathematical Society, 2001. doi:10.1090/conm/280/4620.
- [42] S. V. Dolgov, B. N. Khoromskij, I. V. Oseledets, and D. V. Savostyanov. Computation of extreme eigenvalues in higher dimensions using block tensor train format. *Computer Physics Communications*, 185(4):1207–1216, 2014. doi:10.1016/j.cpc.2013.12.017.
- [43] G. W. Stewart and J. Sun. *Matrix perturbation theory*. Computer science and scientific computing. Academic Press, 1990.
- [44] M. K. Scherer, B. Trendelkamp-Schroer, F. Paul, G. Pérez-Hernández, M. Hoffmann, N. Plattner, C. Wehmeyer, J.-H. Prinz, and F. Noé. PyEMMA 2: A software package for estimation, validation, and analysis of Markov models. *Journal of Chemical Theory and Computation*, 11(11):5525–5542, 2015. doi:10.1021/acs.jctc.5b00743.
- [45] G. R. Bowman, V. S. Pande, and F. Noé, editors. *An introduction to Markov state models and their application to long timescale molecular simulation*. Springer Netherlands, 2014. doi:10.1007/978-94-007-7606-7.
- [46] K. Lindorff-Larsen, S. Piana, R. O. Dror, and D. E. Shaw. How fast-folding proteins fold. *Science*, 334(6055):517–520, 2011. doi:10.1126/science.1208351.

- [47] L. Boninsegna, R. Banisch, and C. Clementi. A data-driven perspective on the hierarchical assembly of molecular structures. *Journal of Chemical Theory and Computation*, 14(1):453–460, 2017. doi:[10.1021/acs.jctc.7b00990](https://doi.org/10.1021/acs.jctc.7b00990).
- [48] G. Pérez-Hernández, F. Paul, T. Giorgino, G. De Fabritiis, and F. Noé. Identification of slow molecular order parameters for Markov model construction. *Journal of Chemical Physics*, 139(1):15102, 2013. doi:[10.1063/1.4811489](https://doi.org/10.1063/1.4811489).
- [49] P. Deuffhard and M. Weber. Robust Perron cluster analysis in conformation dynamics. *Linear Algebra and its Applications*, 398:161–184, 2005. doi:[10.1016/j.laa.2004.10.026](https://doi.org/10.1016/j.laa.2004.10.026).
- [50] G. Froyland and K. Padberg. Almost-invariant sets and invariant manifolds — Connecting probabilistic and geometric descriptions of coherent structures in flows. *Physica D*, 238:1507–1523, 2009. doi:[10.1016/j.physd.2009.03.002](https://doi.org/10.1016/j.physd.2009.03.002).